Review

Recent Trends in Graphitic Carbon Nitride-Based Binary and Ternary Heterostructured Electrodes for Photoelectrochemical Water Splitting

Ravindranadh Koutavarapu [1] , **Shaik Gouse Peera** [2] , **Tae Gwan Lee** [2], **Chimpiri Rao Myla** [3,*], **Dong-Yeon Lee** [1,*], **Jaesool Shim** [4,*] **and Suresh Kannan Balasingam** [5,*,†]

1   Department of Robotics and Intelligent Machine Engineering, College of Mechanical and IT Engineering, Yeungnam University, Gyeongsan 712-749, Korea; ravindra_physicist@ynu.ac.kr
2   Department of Environmental Science and Engineering, Keimyung University, Daegu 42602, Korea; gouse@kmu.ac.kr (S.G.P.); wateree@naver.com (T.G.L.)
3   Department of Physics, Andhra Loyola College, Vijayawada 520-008, Andhra Pradesh, India
4   School of Mechanical Engineering, Yeungnam University, Gyeongsan 712-749, Korea
5   Department of Materials Science and Engineering, Faculty of Natural Sciences, Norwegian University of Science and Technology (NTNU), 7491 Trondheim, Norway
*   Correspondence: raomc72@gmail.com (C.R.M.); dylee@ynu.ac.kr (D.-Y.L.); jshim@ynu.ac.kr (J.S.); suresh.k.balasingam@ntnu.no or suresh@korea.ac.kr (S.K.B.)
†   Current address: Graduate School of Energy and Environment (KU-KIST Green School), Korea University (KU), Seoul 136-713, Korea.

Abstract: The graphitic carbon nitride (g-C$_3$N$_4$) is a class of two-dimensional layered material. The ever-growing research on this fascinating material is due to its unique visible light absorption, surface, electrocatalytic, and other physicochemical properties that can be useful to different energy conversion and storage applications. Photoelectrochemical (PEC) water splitting reaction is one of the promising applications of g-C$_3$N$_4$, wherein it acts as a durable catalyst support material. Very recently, the construction of g-C$_3$N$_4$-based binary and ternary heterostructures exhibited superior PEC water splitting performance owing to its reduced reunion of e-/h+ pairs and the fast transfer of charge carriers at the heterostructure interface. This review compiles the recent advances and challenges on g-C$_3$N$_4$-based heterostructured photocatalysts for the PEC water splitting reaction. After an overview of the available literature, we presume that g-C$_3$N$_4$-based photocatalysts showed enhanced PEC water splitting performance. Therefore, it is believed that these materials have tremendous opportunities to act as durable catalyst support for energy-related applications. However, researchers also considered several limitations and challenges for using C$_3$N$_4$ as an efficient catalyst support material that must be addressed. This review article provides an overview of the fundamental principles of PEC water splitting, the current PEC water splitting research trends on g-C$_3$N$_4$-based binary and ternary heterostructured electrodes with respect to different electrolytes, and the other key factors influencing their photoelectrochemical performance. Finally, the future research direction with several recommendations to improve the photocatalytic efficiency of these materials is also provided at the end.

Keywords: g-C$_3$N$_4$; binary and ternary heterostructures; photoelectrochemical water splitting; hydrogen; photocatalyst

1. Introduction

With the rapid industrial developments and the expanding global population, the energy demand is constantly increasing, which has posed a significant threat to human life [1,2]. Furthermore, the extensive use of fossil fuels and industrial waste has led to a tremendous increase of greenhouse gases in the atmosphere [3,4]. On the other hand, renewable energy technologies such as wind, solar, and tidal energy have great potential

for future generations [5]. Among these, solar energy is considered the most promising one, due to its earth abundance and non-hazardous nature [6]. However, the wavelength of solar illumination reaching the earth is greater than 340 nm, containing only a small portion of UV light (<3%) and a large amount of visible light in the range of 400–800 nm. Therefore, the design and synthesis of suitable visible-light active semiconductor materials having a small bandgap are essential to harvest the abundant solar energy for photocatalytic and other renewable energy-related applications [6,7].

Hydrogen is an attractive green fuel that can be used for many different applications, such as heating, driving vehicles, and material refining [8,9]. Hydrogen has the potential to replace fossil fuels due to its highest energy density and the possibility to use in internal combustion engines and fuel cells, which will be the future for emission-free transportation [10–12]. Moreover, different water splitting techniques have been introduced for hydrogen production, such as electrochemical, thermochemical, photocatalytic, photoelectrochemical (PEC), and biological hydrogen production [13,14]. Among them, PEC water splitting is one of the ways to utilize solar energy for hydrogen generation, which can be further used for many other energy-related applications. [15,16]. Nevertheless, hydrogen production via PEC water splitting is one of the promising methods due to its safety factors, non-toxicity, and the final reaction that produces pure hydrogen and oxygen without any byproducts [17,18].

1.1. Fundamental Concepts of Semiconductor-Mediated Heterogeneous Photocatalysis

Semiconductor-based nanostructures have received significant attention in recent years for energy and environmental applications due to their cost-effective and straightforward synthesis process, and mainly they have nanograins of different sizes and different kinds of heterostructured materials [19,20]. Further, the pristine semiconductor photocatalysts have exhibited minimal PEC water splitting abilities due to their rapid reunion of charge carriers and having a lower surface area [21,22]. Thus, a combination of various semiconductor materials with different morphologies can increase the performance in the visible-light range of the solar spectrum. Moreover, the coupled heterostructured materials with two or more components should have different energy levels that can play an essential role in the interfacial charge transfer of the electron (e^-) and holes (h^+) for the reduction and oxidation of water molecules on the surface of heterostructured electrodes to achieve a higher PEC water splitting activity [23,24].

In recent years, the graphitic carbon nitride (g-C_3N_4) semiconductor-based binary and ternary heterostructured materials have acted as promising photocatalysts for the PEC water splitting and photocatalytic pollutant removal applications [25–27]. Therefore, several investigations have been done on g-C_3N_4-based heterostructured photocatalysts for the PEC water splitting application. Moreover, the heterostructured electrodes are found as an attractive candidate due to their enhanced properties (such as larger surface area, active reactive sites, and higher light absorption capacity) when compared to their bulk counterparts [28,29]. In the case of a g-C_3N_4-based heterostructured electrode, the suitable band edge potentials of the conduction band (CB) and valence band (VB) of different nanostructured semiconductor materials with various morphologies are combined with g-C_3N_4, which could facilitate the charge transfer kinetics of photogenerated e^-/h^+ through the interfacial contact. Moreover, the solar-light active nanostructured materials upon the irradiation generate reactive oxygen species, and it also assists in suppressing the recombination rate of photogenerated e^-/h^+ pairs [30,31]. Therefore, in heterostructured photocatalysts, the assembly of heterojunction could improve the photocatalytic reactions due to its extended absorption of light, synergistic interactions with facile charge transportation, and the reduced recombination rate of charge carriers [32,33].

1.2. The Graphitic Carbon Nitride (g-C_3N_4) Material

The g-C_3N_4 is a kind of strong allotrope of carbon nitride family having a bandgap of around 2.7 eV, and typically it is in the form of two-dimensional (2D) nanosheets comprising

of tri-s-triazines interlayers [34]. The g-C$_3$N$_4$ is one of the graphite-like layered structure materials (shown in Figure 1) with superior prospects due to their ease of availability, low price, and environmental friendliness [35].
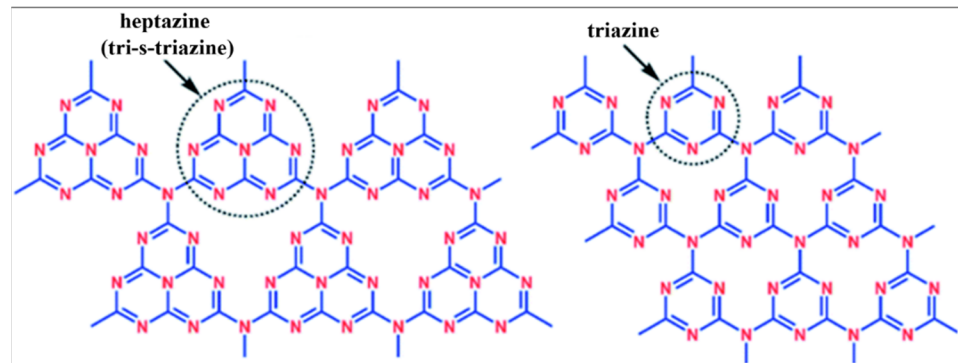

Figure 1. Two fundamental structural units of g-C$_3$N$_4$. Reprinted with permission from reference [36], Copyright 2018, Royal Society of Chemistry.

The g-C$_3$N$_4$ molecular surface contains a large number of π-conjugated planar layers, which have an excellent complexing effect with high stability, so the material has been used for photocatalytic and PEC applications in recent years [37]. However, because of the utilization of only visible light, fast recombination of e$^-$/h$^+$ pairs, low charge separation efficiency, and the moderate specific surface area, it can provide fewer active sites, which reduces its effective usage as a pristine photocatalyst [38,39]. Thus, in order to avoid these disadvantages, the design and synthesis of g-C$_3$N$_4$-based semiconductor heterostructures with appropriate photocatalytic properties could be an effective approach for enhancing the PEC water splitting efficiency [40,41].

1.3. Basic Principles of PEC Water Splitting

The increased accumulation of greenhouse gases has resulted in a constant increase in the global average temperature, enabling a shift in perspective and redirecting the focus from carbon-based energy resources to carbon-free renewable energy technologies [42,43]. In this context, PEC water splitting has foremost importance, in that it generates only H$_2$ and O$_2$ at two electrodes without any other polluting gases [5,44]. The schematic representation of the PEC water splitting mechanism is presented in Figure 2.
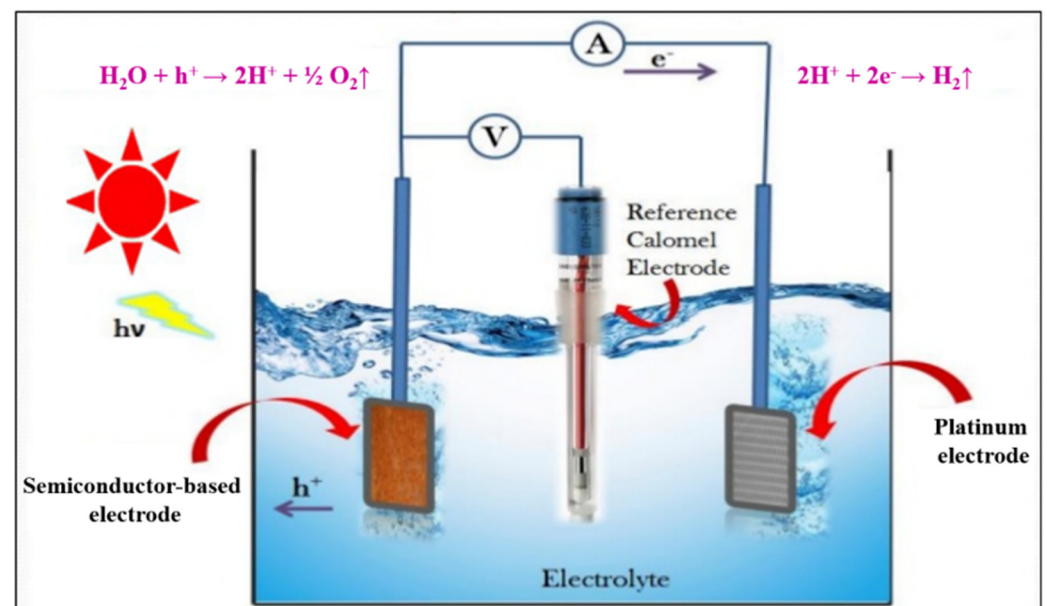
Figure 2. Schematic representation of PEC water splitting mechanism.

Moreover, the PEC-based experiments are performed at room temperature, and the semiconductor electrodes are fabricated using inorganic compounds, which are stable in aqueous electrolytes. In contrast, organic-based semiconductor electrodes show poor stability in PEC water splitting reactions [45,46]. The PEC water splitting device employs quantum solar energy conversion materials in which the semiconductor absorbs incoming photons, resulting in the electron–hole pairs generation process. The incident sunlight on the photoanode excites electrons from the valence band to the conduction band, leaving behind holes in the valence band of semiconductor material [47]. Further, the charge separation typically occurs by the migration of carriers under the influence of the electric field, and the charge transfer occurs at the semiconductor/electrolyte interface. In a photoelectrode, the minority carriers are transported to the electrochemical interface in order to drive the reaction. For a photoanode, holes oxidize water molecules, and for a photocathode, electrons reduce the H^+ ions at the electrode surface [48].

For the past few years, solar-driven visible-light active semiconductor materials were combined with g-C_3N_4, which showed a better PEC water splitting performance due to their enhanced light absorption ability, robust synergistic interface, the enlarged surface area, and the effective separation of e^-/h^+ pairs [49]. Furthermore, these g-C_3N_4-based binary and ternary heterostructured electrodes with various morphologies can significantly progress the movement of charge carriers at the electrode/electrolyte interface and, in turn, enhance the PEC water splitting efficiency. However, despite these recent signs of progress, critical reviews on g-C_3N_4-based binary and ternary heterostructured photoelectrodes for the PEC water splitting reaction are still lacking. Therefore, this review summarizes the different types of g-C_3N_4-based binary and ternary heterostructured photoelectrodes used for PEC water splitting reaction, along with their advantages and limitations.

## 2. Importance of g-C_3N_4-Based Hybrid Heterostructured Electrodes

Generally, when the pristine g-C_3N_4 is subjected to light, it absorbs photons and subsequently generates the photo-induced e^-/h^+ pairs. However, the excited electrons in the CB are in a most unstable state and will tend to occupy the stable state, thus coming back to the VB and recombining with photogenerated holes [50]. Therefore, to suppress the recombination of charge carriers and achieve maximum efficiency, g-C_3N_4 should combine with other semiconductor photocatalysts through the formation of heterostructured electrodes [51]. Recently, some approaches have been introduced to enhance the solar-driven visible-light active photocatalytic performance of g-C_3N_4 materials. For instance, the construction of heterostructured electrodes with g-C_3N_4 and other semiconductors, doping with metals and non-metals, and the fabrication of mesoporous heterostructures [52–54]. Among them, the construction of g-C_3N_4-based binary and ternary heterostructured electrodes exhibited a superior PEC activity due to its reduced reunion of electron–hole pairs and the quick transfer of charge carriers at the interface of the heterostructured electrodes. Furthermore, while developing g-C_3N_4-based heterostructured electrodes, g-C_3N_4 should associate with both the visible and UV light-based semiconductor materials, which could enlarge the absorption of the solar spectrum to the maximum range [55,56].

3. g-C_3N_4-Based Binary Heterostructured Photoelectrodes for PEC Water Splitting

The pristine g-C_3N_4 material has limitations such as fast e^-/h^+ reunion rate, restricted to visible-light absorption range, and the moderate surface area, which urges the development of new approaches to enhance its applications [57,58]. To overcome the above limitations and achieve greater efficiencies, g-C_3N_4-based binary heterostructures have been constructed, and some of them are reported here. Binary heterostructures of g-C_3N_4, along with various concentrations of MnO_x (2, 5, 7, 10, and 15%), were synthesized via in-situ thermal decomposition method to enhance the PEC activity [59]. The XRD result showed that the hexagonal phase of g-C_3N_4, the monoclinic phase of MnO_x, and the heterostructure formation did not affect the individual components. The morphology results established that the irregular-shaped MnO_x nanoparticles (NPs) dispersed over the

g-C$_3$N$_4$ surface. The visible-light-harvesting ability of an electrode was enhanced by the formation of heterostructure when compared to pristine samples. From the electrochemical impedance spectroscopy (EIS) results, the 10% MnO$_x$/g-C$_3$N$_4$ heterostructured electrode exhibited the lowest charge transfer resistance (R$_{ct}$) compared to the remaining samples. Further, the 10% MnO$_x$/g-C$_3$N$_4$ heterostructured electrode showed a higher photocurrent density (0.003 A cm^{-2} at 1.25 V vs. Ag/AgCl) than the remaining photoanodes. Thus, the synergistic interactions among g-C$_3$N$_4$ and MnO$_x$ can effectively progress the mobility of charge carriers and diminish the reunion of e$^-$/h$^+$ pairs, which enhances the PEC performance. Wang et al. successfully constructed a core-shell g-C$_3$N$_4$@ZnO (CN/ZN) heterostructured electrode with different amounts of g-C$_3$N$_4$ (0.01, 0.05, 0.10, 0.15, 0.20 g) using a facile reflux technique [60]. The XRD results (Figure 3a) confirmed the hexagonal phase of ZnO and the interlayer stacking of CN units with no impurity phases. The morphology studies (Figure 3b) showed the heterostructure formation with an effective distribution of ZnO NPs over the CN surface. When compared to the pristine ZnO, the visible-light absorption ability of the CN/ZN heterostructured electrode (Figure 3c) is enhanced through the formation of heterostructures. The EIS results (Figure 3d) demonstrated that the CN/ZN-0.15 heterostructured electrode exhibited the lowest charge-transfer resistance (R$_{ct}$) among all samples. From the transient photocurrent (*I-t*) results (Figure 3e), the CN/ZN-0.15 photoelectrode exhibited a sharp increase of photocurrent density with a quick photoresponse than the other samples. Furthermore, the CN/ZN-0.15 photoelectrode provided a highest photocurrent density at 1.5 V vs. SCE in 0.1 M Na$_2$SO$_4$ electrolyte under visible-light illumination. This improvement in the PEC water splitting activity (Figure 3f) is owed to the core-shell morphology, higher light absorption capability, formation of synergistic interfaces, and the facile charge carrier transport.

Xiao et al. successfully constructed a binary heterostructured electrode in which zero-dimensional (0D) g-C$_3$N$_4$ NPs covered over the one-dimensional (1D) TiO$_2$ nanotube arrays with an interfacial oxygen vacancy layer (CN/OV-TO). This heterostructured electrode was synthesized using anodic oxidation followed by the reduction and vapor deposition processes [61]. The visible-light-harvesting ability is improved substantially after forming the heterostructure and oxygen vacancies (OV) associated with CN, TO, and CN/TO. The structural and morphology investigations confirmed the formation of 0D/1D heterostructured electrodes. Further, the EIS results demonstrated that the constructed CN/OV-TO heterostructured electrode exhibited the smallest R$_{ct}$ value among all prepared samples. In addition, the photocurrent density of CN/OV-TO photoanode is around 0.72 mA cm^{-2} at 1.23 V Vs. RHE under visible-light illumination. This value is almost eight times higher than the CN/TO heterostructured electrode without an interfacial OV layer. This enhanced water splitting ability was attributed to the Z-scheme mechanism along with the interfacial OV layer, which delays the reunion of e$^-$/h$^+$ pairs and endorses the facile charge carrier transport mechanism. Reddy et al. constructed 1D ZnWO$_4$ nanorods decorated over the 2D g-C$_3$N$_4$ nanosheets using a facile hydrothermal synthesis method to enhance the PEC water splitting reaction under solar light [62]. By the formation of the heterostructured electrode, the solar light-harvesting capability was remarkably improved. The crystal phase and morphology analysis confirmed the formation of the heterostructured electrode by the successful decoration of ZnWO$_4$ nanorods on the surface of g-C$_3$N$_4$ nanosheets. Further, the EIS results validated that the constructed 2D/1D heterostructured electrodes exhibited the lowest R$_{ct}$ value when compared to pristine samples. Moreover, the photocurrent density of the 2D/1D heterostructured electrode is almost 6.75 times and 3.31 times higher than the pristine ZnWO$_4$ and g-C$_3$N$_4$ electrodes, respectively. Nevertheless, the 2D/1D heterostructured electrode exhibited a very good stability and thus the formation of a binary heterostructured electrode could effectively improve the migration of charge carriers with a lower charge transfer resistance and suppress the reunion of e$^-$/h$^+$ charge carriers.
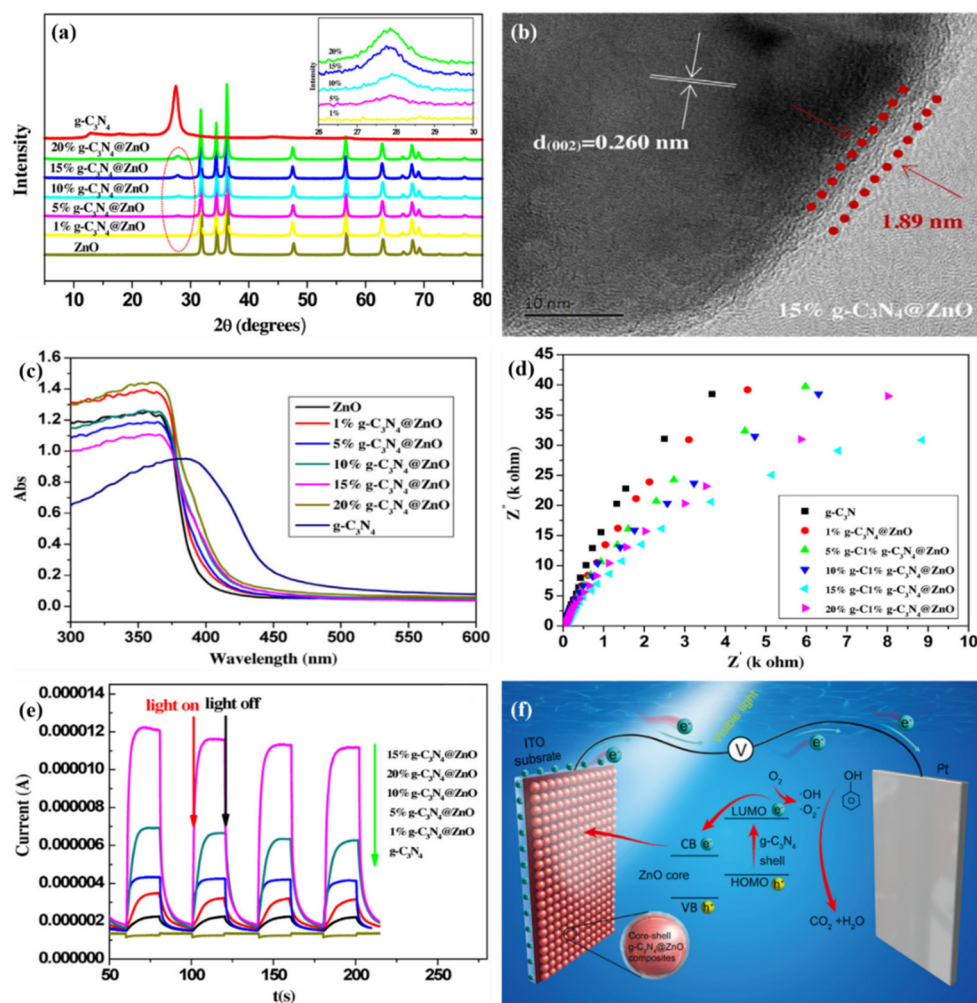
Figure 3. (**a**) XRD patterns, (**b**) HRTEM image of 15%CN@ZO material, (**c**) optical absorption spectra, (**d**) Nyquist plots, (**e**) *I-t* curves, and (**f**) charge transfer mechanism of the CN@ZO heterostructured electrode. Reprinted with permission from reference [60], Copyright 2017, Elsevier.

A novel hybrid carbon-doped CuO/g-C_3N_4 (C-CuO/CN) heterostructured electrode was prepared using a facile one-step microwave-supported approach to improve the PEC performance under visible source [40]. The crystal phase results confirmed the formation of the monoclinic phase of CuO and the interlayer stacking of the CN units. The morphology results demonstrated that the CuO seems to be an evenly dispersed micro-flowers consisting of intermixed ultrathin nanosheets and distributed over the surface of CN. The photoluminescence spectra of C-CuO/CN heterostructured material showed a very weak intensity compared to the CuO, CN, and CuO/CN materials, and this enhanced PL activity can be ascribed to the significance of carbon dopant, which influences lattice defects. The C-CuO/CN heterostructured electrode exhibited the lowest charge transfer resistance of 3.48 kΩ cm^{-2} than the CuO (18.53 kΩ cm^{-2}) and CuO/CN (7.69 kΩ cm^{-2}) electrodes. Furthermore, the photocurrent density of the C-CuO/CN electrode is around -2.85 mA cm^{-2} at 0 V vs. RHE under visible source, and it is around 227% and 38% higher than the CuO and CuO/CN electrodes, respectively. Thus, the carbon-doping, influence of lattice defects, and the formation of interfacial interactions significantly enhanced the PEC performance.

Seza and co-workers successfully constructed novel photoelectrodes made of SnO_2 NPs (various loading of 0.175, 0.6, and 1 g) decorated over the surface of porous g-C_3N_4 nanosheets (CN/SN) using a facile microwave synthesis method [63]. The XRD results demonstrated that the CN/SN heterostructured material exhibited both the g-C_3N_4

and SnO$_2$ phases. The morphology results showed the highly porous structure of CN nanosheets and the irregular shape of SnO$_2$ NPs. The light absorption capacity of heterostructured CN/SN electrode enhanced towards the visible-active region compared to the pristine samples. The CN/SN-0.175 heterostructured electrode exhibited the highest specific surface area of 195 m^2 g^{-1} compared to the other samples. From the linear sweep voltammetry (LSV) results, the CN/SN-0.175 heterostructured electrode showed a photocurrent density of 0.033 mA cm^{-2} at 1.2 V vs. Ag/AgCl in 0.2 M Na$_2$SO$_4$ electrolyte under visible-light irradiation, and this photocurrent value is superior to the remaining photoelectrodes. This enhanced PEC performance can be ascribed to the formation of porous nanosheets, enhanced visible-light absorption ability, and the formation of the interfacial heterostructure.

Novel binary g-C$_3$N$_4$ combined with carbon nanotubes (CN/CT) heterostructured film was systematically fabricated on the FTO substrate using a facile polycondensation method to enhance PEC water splitting ability [52]. The structural and morphological analysis evidence the formation of CN/CT heterostructured electrodes with synergistic interfaces. As a result, the light-harvesting capacity systematically improved towards the visible-active region by the development of heterostructure. Further, the EIS results validated that the constructed CN/CT heterostructured electrode showed the lowest charge transfer resistance of 6.5 × 10^5 Ω, and it is around 9.3 times higher than the pristine CN electrode. The photocurrent density of the CN/CT heterostructured electrode showed 0.075 mA cm^{-2} at 1 V vs. Ag/AgCl under visible light, and it is around 11 times superior to the pure CN photoanode. Thus, combing CN with CT significantly enhanced the electron conductivity, light-harvesting ability, and the separation of charge carriers, which further improved the PEC water splitting efficiency. Bakr and co-workers successfully constructed a binary Z-scheme heterostructured electrode using α-Fe$_2$O$_3$ nanotubes combined with various concentrations (1, 2, and 3.75 wt.%) of ruptured tubular g-C$_3$N$_4$ (FO/CN) using an electrostatic self-assembly technique [64]. The XRD results revealed that both crystal phases were presented in the FO/CN heterostructured electrode. The morphology results showed that the α-Fe$_2$O$_3$ nanotubes were anchored over the tubular g-C$_3$N$_4$, and the bandgap modification was detected for the FO/CN heterostructured material. The EIS results exhibited the lowest charge transfer resistance value for FO/CN-1 sample. Furthermore, the FO/CN-1 heterostructured electrode showed the highest photocurrent density of 0.0055 mA cm^{-2} at 1 V vs. SCE in 0.1 M Na$_2$SO$_4$ electrolyte under sunlight. This improvement in the PEC performance was due to the morphological interfaces, heterostructure formation, and quick transportation of charge carriers.

Novel binary heterostructured electrodes made of BiOI nanoplates combined with multilayered g-C$_3$N$_4$ (BI/CN-M) and few-layered g-C$_3$N$_4$ nanosheets (BI/CN-S) were systematically synthesized using a simple solvothermal technique for the enhancement of PEC water splitting reaction [65]. The XRD results showed the formation of the tetragonal phase of BiOI and the interlayer stacking of CN, and both crystal phases have appeared in the BI/CN-S heterostructured electrode. The morphology results demonstrated that the BI nanoplates were decorated over the CN-S nanosheets, which confirmed the establishment of the heterostructured material. Further, the FTIR and Raman spectra results evidently showed the synergistic interactions among BI and CN materials. From the EIS results, the BI/CN-S heterostructured electrode showed the lowest charge transfer resistance than the pure BI, CN, and BI/CN-M electrodes. Moreover, the observed photocurrent density of BI/CN-S heterostructured electrode was around 0.20 mA cm^{-2} at −0.5 V vs. Ag/AgCl in 0.1 M Na$_2$SO$_4$ under visible-light irradiation, and the current density value was superior to BI/CN-M (0.16 mA cm^{-2}), BI (0.09 mA cm^{-2}), CN-M (0.05 mA cm^{-2}), and CN-S (0.04 mA cm^{-2}) electrodes. The enhanced water-splitting ability of the heterostructure material was attributed to the enlarged light absorption ability, the diminished reunion of charge carriers, and the synergistic trap passivation in the heterostructured electrode.

Liu and colleagues constructed the well-designed TiO$_2$ nanotube arrays (TNTAs) and dispersed the g-C$_3$N$_4$ nanoparticles over TNTAs using anodic oxidation followed by calci-

nation methods [66]. The formation mechanism of g-C$_3$N$_4$/TNTAs (CN-TN) heterojunction was schematically represented in Figure 4a. The crystallographic results showed the anatase phase of TiO$_2$ and interlayer stacking of g-C$_3$N$_4$, which significantly confirmed the formation of heterojunctions. The morphology results from Figure 4b–d showed that the g-C$_3$N$_4$ nanosheets covered the walls of the TiO$_2$ nanotubes. From the LSV results (Figure 4e), the photocurrent density of CN-TN electrode was observed around 0.86 mA cm^{-2} and is nearly double that of pure TNTAs electrode. The transient photocurrent (I-t) results (Figure 4f) demonstrated that the CN-TN heterojunction electrode exhibited a sharp increase of photocurrent density with a quick photoresponse compared to the as-prepared pristine samples. The charge transfer resistance of the CN-TN heterojunction electrode (Figure 4g) was significantly reduced among the other samples under light illumination. Thus, the formation of binary heterojunction between g-C$_3$N$_4$ and TNTAs (Figure 4h) could significantly enhance the transportation of charge carriers and reduce the reunion of photo-induced e$^-$/h$^+$ pairs, which in turn enhanced the PEC water splitting efficiency.
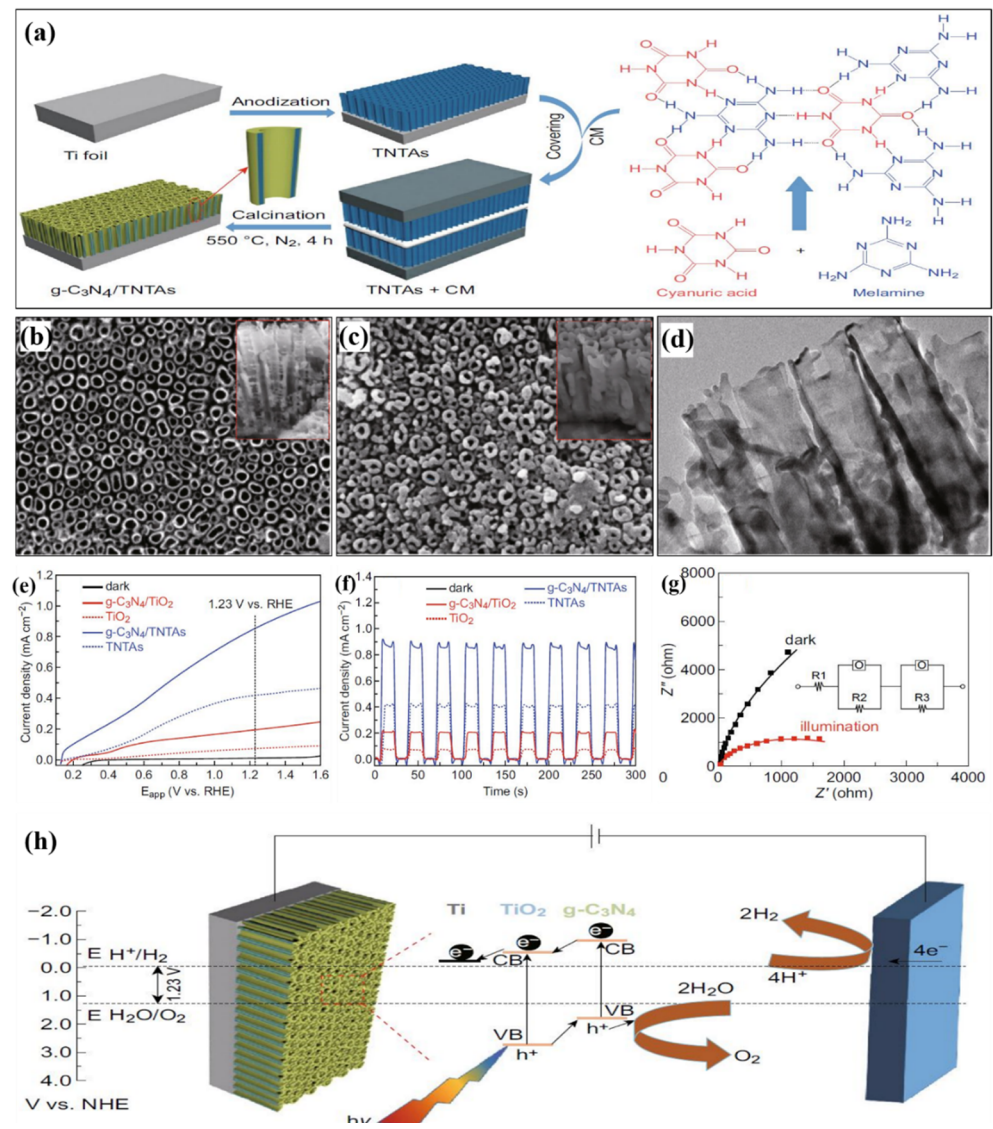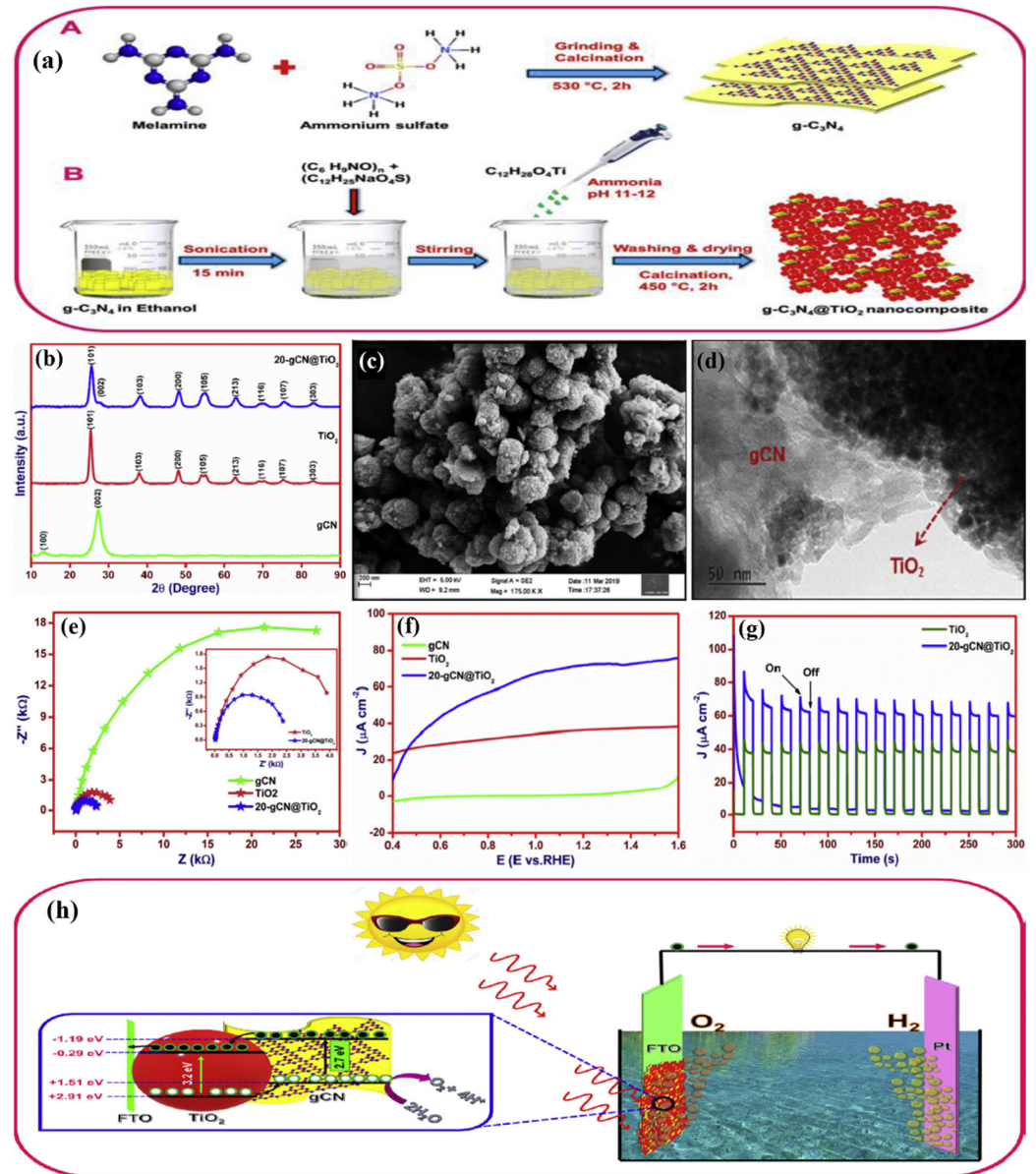

Figure 4. (**a**) Formation mechanism of CN-TN heterojunction, SEM images of (**b**) TNTAs, (**c**) CN-TN heterojunction, (**d**) TEM image of CN-TN heterojunction, (**e**) LSV curves, (**f**) *I-t* curves, (**g**) Nyquist plots, and (**h**) charge transfer mechanism of the CN-TN heterojunction. Reprinted with permission from reference [66], Copyright 2018, Springer.

Liu and co-workers effectively fabricated the g-C_3N_4-coated Fe_2O_3 nanoplatelets (CN/FO) electrodes using the facile electrodeposition followed by chemical vapor deposition methods [67]. The morphology and structural results demonstrated the distribution of g-C_3N_4 nanoparticles over the surface of Fe_2O_3 nanoplatelets. Further, the light-harvesting ability was significantly enhanced after the formation of CN/FO heterostructuredelectrode, and the PL intensity was diminished when compared to the pure CN and FO electrodes. From the EIS analysis, the CN/FO heterostructured photoanode showed the lowest R_{ct} value compared to the remaining photoanodes. The photocurrent density of the CN/FO heterostructured electrode showed around 0.78 mA cm^{-2} at 0.4 V vs. Ag/AgCl in 1.0 M NaOH under visible light, and it is around 70 times higher than the pure FO photoanode. Therefore, the introduction of CN over the surface of FO considerably enriched the light-harvesting ability, separation of e$^-$/h$^+$ pairs, and quicker interfacial charge transfer, which improved the water-splitting ability. Novel binary 2D/2D heterostructured electrode composed of porous g-C_3N_4 and BCN nanosheets (CN/BCN) was successfully fabricated using a facile thermal polymerization technique [68]. The XRD results demonstrated that both the crystal phases of CN and BCN were presented in the CN/BCN heterostructured electrode. The morphology results showed that the porous CN nanosheets were anchored over the BCN nanosheets. From differential reflectance spectroscopy (DRS) results, the loading of CN towards BCN could substantially enhance the light-harvesting capability. The charge transfer resistance of CN/BCN electrode was around 2.8 kΩ, which is 11 times and five times lesser than CN and BCN electrodes, respectively. Further, the transient photocurrent density of the CN/BCN electrode is higher than the individual CN and BCN electrodes. Moreover, the CN/BCN heterostructured electrodes showed a photocurrent density of 0.62 mA cm^{-2} at 0.62 V vs. Ag/AgCl in 0.1 M Na_2SO_4 electrolyte under visible-light illumination, which was around 8 and 3 times higher than the CN (0.08 mA cm^{-2}) and BCN (0.21 mA cm^{-2}) electrodes, respectively. Thus, the morphological 2D interfaces, superior migration of charge carriers, and the separation of e$^-$/h$^+$ pairs significantly enhanced the PEC water splitting performance.

Murugan and colleagues systematically fabricated a binary g-C_3N_4/TiO_2 (CN/TO) heterostructured electrode with different concentrations of CN (5, 10, 15, 20, and 25 wt.%) using a facile in-situ soft template technique (Figure 5a) for the improvement of PEC water splitting performance [69]. The XRD results (Figure 5b) confirmed the anatase phase of TiO_2, the interlayer stacking of CN, and both the phases have appeared in the CN/TO heterostructured electrode. The morphology results (Figure 5c,d) demonstrated that the TO NPs were decorated over the CN nanosheets. From the EIS analysis (Figure 5e), the CN/TO-20 photoanode showed the lowest R_{ct} value than the remaining photoanodes. Furthermore, the photocurrent density (Figure 5f–g) of CN/TO-20 heterostructured electrode was around 0.0723 mA cm^{-2} at 1.23 V vs. RHE in 1 M KOH electrolyte under visible-light and the photocurrent density value was superior than the CN (0.00082 mA cm^{-2}), TO (0.0366 mA cm^{-2}), CN/TO-5 (0.0472 mA cm^{-2}), CN/TO-10 (0.0544 mA cm^{-2}), CN/TO-15 (0.0632 mA cm^{-2}), and CN/TO-25 (0.0658 mA cm^{-2}) electrodes. The enhanced water splitting ability was accounted for their enlarged light absorption ability, the diminished reunion of charge carriers, and synergistic interfacial effect in the heterostructured electrode. The same group, Murugan and co-workers, successfully fabricated a binary combination of hierarchical Bi_2MoO_6 and various amounts (1, 3, 5, 7, 10, and 12 wt.%) of g-C_3N_4 (BMO/CN) using a solvothermal technique for the enhancement of PEC water splitting ability [70]. The XRD results revealed the formation of the orthorhombic phase of BMO, the interlayer stacking of CN, and both the phases have appeared in the BMO/CN heterostructured electrode. The regulation of the bandgap was detected for the BMO/CN heterostructured electrode compared to the pure samples, which enlarged the visible-light-harvesting capability. From the EIS analysis, the BMO/CN-10 heterostructured electrode showed the lowest R_{ct} value, the photocurrent density of the BMO/CN-10 electrode was around 0.0212 mA cm^{-2} at 1.23 V vs. RHE in 1 M KOH electrolyte under visible-light illumination, and the photocurrent density value was about 28 and 7 times greater than the pristine CN and BMO electrodes,

respectively. Thus, heterostructure formation significantly enhanced the light-harvesting ability, separation of e^-/h^+ pairs, and quicker interfacial charge transfer, which progressed the water-splitting ability.
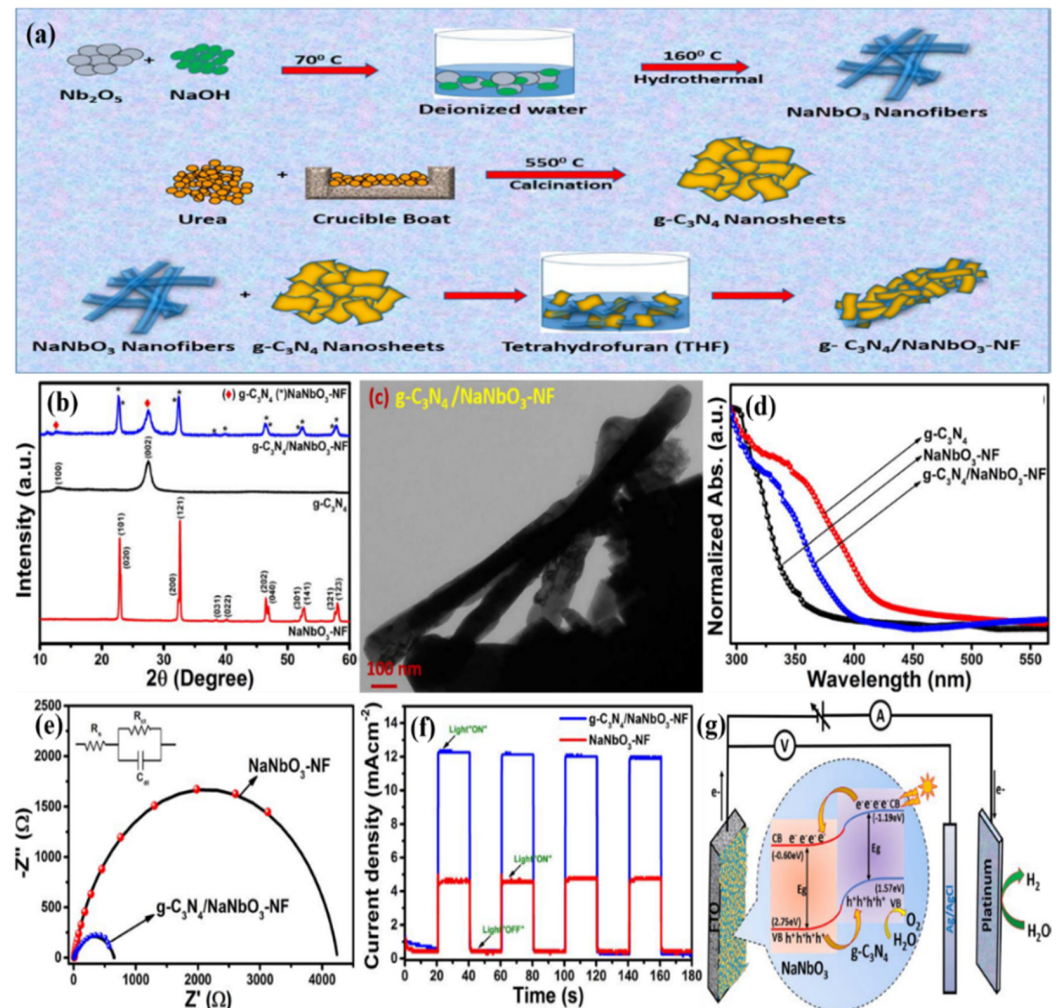

Figure 5. (**a**) Formation mechanism of CN@TO heterostructured material, (**b**) XRD patterns, (**c**) SEM image of 20-CN@TO material, (**d**) TEM image of 20-CN@TO material, (**e**) Nyquist plots, (**f**) LSV curves, (**g**) *I-t* curves, and (**h**) charge transfer mechanism of the CN@TO heterostructured electrodes. Reprinted with permission from reference [69], Copyright 2020, Elsevier.

Mohammad et al. successfully fabricated the novel heterostructured electrode using different concentrations (2 and 4 mM) of SnO_2 NPs decorated over the surface of g-C_3N_4 nanosheets (CN/SN) via a simple hydrothermal method [71]. The XRD results confirmed that both the crystal phases of SN (tetragonal rutile phase) and CN were presented in the CN/SN heterostructured electrode without any impurity phases. The FTIR and XPS results established the formation of CN/SN heterostructured electrodes. The visible-light-harvesting ability was significantly enhanced after forming the CN/SN heterostructured electrode, and the PL intensity was diminished compared to the pure CN and SN materials. The CN/SN-4 mM heterostructured electrode demonstrated a higher specific surface area

of 181.54 m^2 g^{-1} than the pure SN (181.13 m^2 g^{-1}) and CN/SN-2 mM (178.69 m^2 g^{-1}) electrodes. From the EIS results, the CN/SN-4 mM heterostructured electrode showed the lowest charge transfer resistance when compared to the pure CN, SN, and CN/SN-2 mM electrodes. Furthermore, the photocurrent density of CN/SN-4 mM photoelectrode was around 2.1 mA cm^{-2} at 1 V vs. Ag/AgCl in 0.2 M Na$_2$SO$_4$ under visible-light and it was around eight times higher than the pure SN electrode. The improved water splitting performance was owing to the enhanced surface area, light absorption ability, diminished reunion of charge carriers, and the synergistic effect in the heterostructured interface.

Kumar et al. successfully constructed heterostructured electrodes made of NaNbO$_3$ nanofibers along with different concentrations (2, 4, and 8 wt.%) of g-C$_3$N$_4$ nanosheets (NNO/CN) using facile hydrothermal followed by chemisorption techniques (Figure 6a) for better PEC water splitting performance [31]. The XRD results (Figure 6b) demonstrated that both the crystal phases of CN (interlayer stacking) and NNO (orthorhombic phase) were presented in the NNO/CN heterostructured electrode. The surface morphology images (Figure 6c) confirmed the effective distribution of NNO nanofibers on the surface of CN nanosheets. The DRS analysis (Figure 6d) showed that the visible-light-harvesting ability was significantly enhanced in the NNO/CN heterostructure electrode. The EIS results (Figure 6e) demonstrated that the NNO/CN-4 photoelectrode exhibited the lowest R$_{ct}$ value, and the *I-t* results (Figure 6f) indicated that the NNO/CN-4 photoelectrode showed a sharp increase of photocurrent density with a quicker photoresponse than the other photoelectrodes. Moreover, the NNO/CN-4 photoelectrode showed a photocurrent density of 12.5 mA cm^{-2} at 1 V vs. Ag/AgCl in 0.5 M NaOH electrolyte under visible-light, which was around three-times higher than the pristine NNO electrode (4.3 mA cm^{-2}). Thus, the formation of heterostructured electrode (Figure 6g) significantly enhanced the light-harvesting ability, separation of e$^-$/h$^+$ pairs, and quicker interfacial charge transfer, which significantly improved the water-splitting ability.

A novel binary heterostructured electrode made of Bi$_2$WO$_6$ quantum dots (QDs) dispersed on the g-C$_3$N$_4$ (CN/BWQ) was prepared by a simplistic in-situ hydrothermal method [72]. The X-ray diffraction results confirmed the interlayer stacking of the CN units and the orthorhombic phase of BW, even after the formation of a heterostructured electrode. Furthermore, the morphological examination revealed that the BW QDs were uniformly distributed over the surface of CN. When compared to the pristine samples, bandgap tuning was observed for the CN/BWQ heterostructured electrode, which significantly enhanced the visible-light-harvesting capability. Moreover, the CN/BWQ heterostructured electrode demonstrated the lowest R$_{ct}$ value, the photocurrent density of CN/BWQ photoanode was observed around 0.39 μA cm^{-2} at 1.23 V vs. RHE under visible-light illumination, and the current density value was about 2.4 and 1.8 times higher than the pristine CN and BWQ electrodes, respectively. Thus, forming a synergistic interfacial heterostructure and the Z-scheme mechanism could significantly enhance the water-splitting activity. The PEC performance of g-C$_3$N$_4$-based various binary heterostructured electrodes is presented in Table 1.

Figure 6. (**a**) Formation mechanism of NNO/CN heterostructured material, (**b**) XRD patterns, (**c**) TEM image of NNO/CN heterostructured material, (**d**) optical absorption spectra, (**e**) Nyquist plots, (**f**) *I-t* curves, and (**g**) charge transfer mechanism of the NNO/CN heterostructured electrode. Reprinted with permission from reference [31], Copyright 2020, IOP.

Table 1. The PEC performance of g-C$_3$N$_4$-based binary heterostructured photoelectrodes.

Photoelectrodes	Synthesis Methods	Potential (V)	Electrolytes	Light Sources	Photocurrent Density (mA cm^{-2})	Ref.
g-C$_3$N$_4$/ZnO	Dip coating	0.5994 vs. RHE	0.5 M Na$_2$SO$_4$	Visible	0.952	[73]
Pt/g-C$_3$N$_4$	Dip coating	0 vs. RHE	0.1 M Na$_2$SO$_4$	Solar	−2.5	[74]
g-C$_3$N$_4$/CoP	Impregnation	0.4 vs. Ag/AgCl	0.05 M Na$_2$SO$_4$	Solar	0.15	[75]
g-C$_3$N$_4$/BiVO$_4$	Hydrothermal	1.23 vs. RHE	1 M KOH	visible	0.021	[76]
g-C$_3$N$_4$/CdS	Electrophoretic and chemical bath deposition	0 vs. Ag/AgCl	0.5 M Na$_2$SO$_3$	Visible	5.4	[77]
g-C$_3$N$_4$/CNTs	Liquid exfoliation	0 vs. SCE	0.5 M Na$_2$SO$_4$	Visible	0.0018	[78]
g-C$_3$N$_4$/SnO$_2$	Pulsing electrophoresis	0.2 vs. Ag/AgCl	0.1 M NaOH	Solar	1.8	[79]
g-C$_3$N$_4$/BiVO$_4$	Sol-gel	-- vs. Ag/AgCl	0.1 M Na$_2$SO$_4$	Solar	0.00046	[80]
g-C$_3$N$_4$/InVO$_4$	Mixing calcination	0.9 vs. Ag/AgCl	0.1 M Na$_2$SO$_4$	Solar	0.013	[81]
g-C$_3$N$_4$/In$_2$S$_3$	Wet chemical	1.5 vs. Ag/AgCl	0.1 M Na$_2$SO$_3$	Visible	0.005	[82]
g-C$_3$N$_4$/Cu$_2$O	Electrophoretic deposition	−0.4 vs. Ag/AgCl	0.1 M NaNO$_3$	Visible	−1.38	[83]

Table 1. *Cont.*

Photoelectrodes	Synthesis Methods	Potential (V)	Electrolytes	Light Sources	Photocurrent Density (mA cm^{-2})	Ref.
Phosphorus doped g-C$_3$N$_4$	Sintering	1.2 vs. Ag/AgCl	0.5 M Na$_2$SO$_4$	Near-infrared	0.0014	[84]
g-C$_3$N$_4$/BiVO$_4$	Electrodeposition	1.23 vs. RHE	0.5 M Na$_2$SO$_4$	Solar	0.42	[85]
g-C$_3$N$_4$/CuO	Co-precipitation	1.2 vs. Ag/AgCl	–	Visible	0.68	[86]
g-C$_3$N$_4$/MoS$_2$	Solvothermal	−0.4 vs. Ag/AgCl	0.1 M PBS	Solar	0.037	[87]
g-C$_3$N$_4$@CuTi	Hydrothermal	0.65 vs. Ag/AgCl	1 M KOH	Visible	0.014	[88]
g-C$_3$N$_4$/LaFeO$_3$	Magnetron sputtering	−0.3 vs. Ag/AgCl	0.1 M Na$_2$SO$_4$	Solar	0.004	[89]
g-C$_3$N$_4$@Si NWs	Metal-assisted etching, and liquid atomic layer deposition	1 vs. Pt	0.5 M Na$_2$SO$_4$	Visible	0.316	[90]
Cobalt doped g-C$_3$N$_4$	Calcination	Ag/AgCl	0.1 M Na$_2$SO$_4$	Solar	0.058	[91]
g-C$_3$N$_4$@CoFe	Solvothermal	0.2 vs. Ag/AgCl	1 M KOH	Visible	0.196	[92]

## 4. g-C$_3$N$_4$-Based Ternary Heterostructured Photoelectrodes for PEC Water Splitting

Numerous efforts have been executed to fabricate g-C$_3$N$_4$-based binary heterostructured electrodes to overcome the constraints and improve the PEC water splitting ability. However, the PEC performance is still limited and not up to the target of practical applications. To overcome these issues, g-C$_3$N$_4$-based complex compounds containing three components have been introduced, and some of the results are discussed here. A novel hybrid ternary anatase TiO$_2$/rutile TiO$_2$/g-C$_3$N$_4$ (A/R/CN) heterostructured electrode was prepared with different mass ratios of CN (20, 30, 40, 50, and 60 mg) using a facile thermoset hybrid technique for the enhancement of water splitting performance [93]. The XRD result confirmed the anatase and rutile phases of TiO$_2$ and the interlayer stacking of the CN units. The electron microscopy results validated that the TiO$_2$ NPs were distributed over the surface of CN, which signifies the formation of a heterostructured electrode. The light-harvesting capacity systematically improved towards the visible region in the case of the ternary heterostructured electrode. From the EIS results, the A/R/CN40 heterostructured electrode showed the lowest charge transfer resistance value than the pure P25, CN, and A/R/CN20, A/R/CN30, A/R/CN50, and A/R/CN60 heterostructured electrodes. Further, the photocurrent density of the A/R/CN40 photoanode was superior to the other electrodes under solar light illumination. Thus, the formation of interfacial interactions among the three components could improve the migration of charge carriers with more separation, which further enhanced the PEC water splitting capability.

Reddy and co-workers have developed a novel ternary electrode made of CdS NPs and Fe$_3$O$_4$ nanocubes dispersed over the g-C$_3$N$_4$ nanosheets (CS/FO/CN) using two-step solvothermal techniques for the enhanced PEC water splitting performance [37]. The morphology results demonstrated that the CdS NPs entered into the Fe$_3$O$_4$ lattices and were distributed on the surface of CN nanosheets. The XRD results confirmed the presence of the hexagonal phase of CdS, the magnetite phase of Fe$_3$O$_4$, the interlayer stacking of CN in CS/FO/CN heterostructured electrode, and the heterostructure formation did not affect the individual phases. The CS/FO/CN electrode showed a superior specific surface area of 40.022 m^2 g^{-1}. Further, the CS/FO/CN ternary heterostructured electrode showed enlarged light-harvesting performance. The charge transfer resistance of CS/FO/CN ternary heterostructured electrode was significantly reduced when compared to CdS, CN@CS, and CS@FO electrodes upon visible-light irradiation. The photocurrent density of the CS/FO/CN ternary heterostructured electrode showed around 0.0238 mA cm^{-2} at 0.2 V vs. Ag/AgCl under visible-light irradiation, and it was around 5.95, 4.76, and 7.93 times higher than CdS, CN@CS, and CS@FO electrodes, respectively. This improvement in the PEC performance was ascribed to the ternary interfacial charge transport, separation efficiency of e$^-$/h$^+$ pairs, and the facile transportation of charge carriers.

Bhandary and colleagues fabricated a bimetallic AgNi alloy surrounded by g-C_3N_4 nanosheets (CN/AgNi) electrodes using a facile one-pot solid-state heat treatment method to improve the PEC water splitting capability [94]. The structural and morphological studies confirmed the heterostructure formation with a successful decoration of bimetallic AgNi alloy over the surface of g-C_3N_4 nanosheets. After the formation of the heterostructure, the light absorption capability remarkably improved. Further, the EIS results confirmed that the constructed CN/AgNi heterostructured electrode showed the lowest R_{ct} value among the pure samples. Furthermore, the CN/AgNi photoelectrode showed the highest photocurrent density of 1.29 mA cm^{-2} at 1.0 V vs. Ag/AgCl in 1.0 M NaOH electrolyte under visible light, and the value was more significant than the CN, CN/Ag, and CN/Ni electrodes. Nevertheless, the CN/AgNi heterostructured electrode exhibited excellent stability, and thus the formation of a heterostructure could effectively improve the migration of charge carriers with lower charge transfer resistance and suppress the reunion of e^-/h^+ pairs.

The novel ternary heterostructured electrodes of Ag_3PO_4/Ag_2MoO_4 materials combined with various concentrations (0.4, 0.8, and 1.2 wt.%) of multilayered g-C_3N_4 nanosheets (AP/AM/CN) were systematically fabricated using the in-situ co-precipitation technique by Liu and colleagues [95]. The XRD results showed the formation of the cubic phase of Ag_3PO_4 and Ag_2MoO_4, the interlayer stacking of CN, and the ternary AP/AM/CN heterostructured electrode contained all three phases. The morphology results demonstrated that both the AP and AM NPs were distributed over the surface of CN nanosheets, which confirmed the establishment of the ternary heterostructured electrode. Further, the FTIR and Raman spectra results evidently showed synergistic interactions among AP/AM and CN interfaces. The visible-light-harvesting ability was considerably enhanced through the formation of ternary AP/AM/CN heterostructured electrodes when compared to the CN, AP, AM, and AP/AM electrodes. From the EIS results, the ternary AP/AM/CN photoanode showed the lowest charge transfer resistance value when compared to the CN, AP, AM, and AP/AM electrodes. Moreover, the photocurrent density of the ternary AP/AM/CN photoelectrode was superior to the other samples under solar light illumination. Thus, the enlarged solar light absorption ability could effectively diminish the reunion of charge carriers and the dual Z-scheme charge carrier pathway that eventually enhanced the PEC water splitting ability.

A novel hybrid ternary g-C_3N_4/Au-SnO_2 QDs (CN/Au/SQD) heterostructured electrode was prepared with different mass ratios of Au-SQD (10, 20, and 30 mg), using calcination and sonication methods (Figure 7a) for the enhancement of PEC water splitting performance [96]. The XRD results revealed the presence of the tetragonal phase of SnO_2, interlayer stacking of the CN units, and the metallic phase of Au. The electron microscopy results (Figure 7b) confirmed that the Au-SQDs were distributed over the surface of CN, which signifies the heterostructure formation. The light-harvesting efficiency (Figure 7c) was systematically improved towards the visible region through the heterostructure formation. The PL spectra (Figure 7d) of CN/Au/SQD heterostructured electrode showed a very weak intensity compared to the SQD, CN, and Au-SQD samples. From the EIS results, the CN/Au/SQD ternary electrode showed the lowest R_{ct} value than the SQD, CN, and Au-SQD electrodes. Furthermore, the CN/Au/SQD photoelectrode displayed the superior photocurrent density (Figure 7e) of 0.0402 mA cm^{-2} at 1.0 V vs. Ag/AgCl in 0.1 M Na_2SO_3 electrolyte under visible-light irradiation, and the value was significantly greater than the SQD, CN, and Au-SQD electrodes. Thus, the fabrication of metal-semiconductor combined with CN ternary heterostructured electrodes (Figure 7f) could improve the migration of charge carriers with more separation efficiency, which further enhanced the PEC water splitting performance.
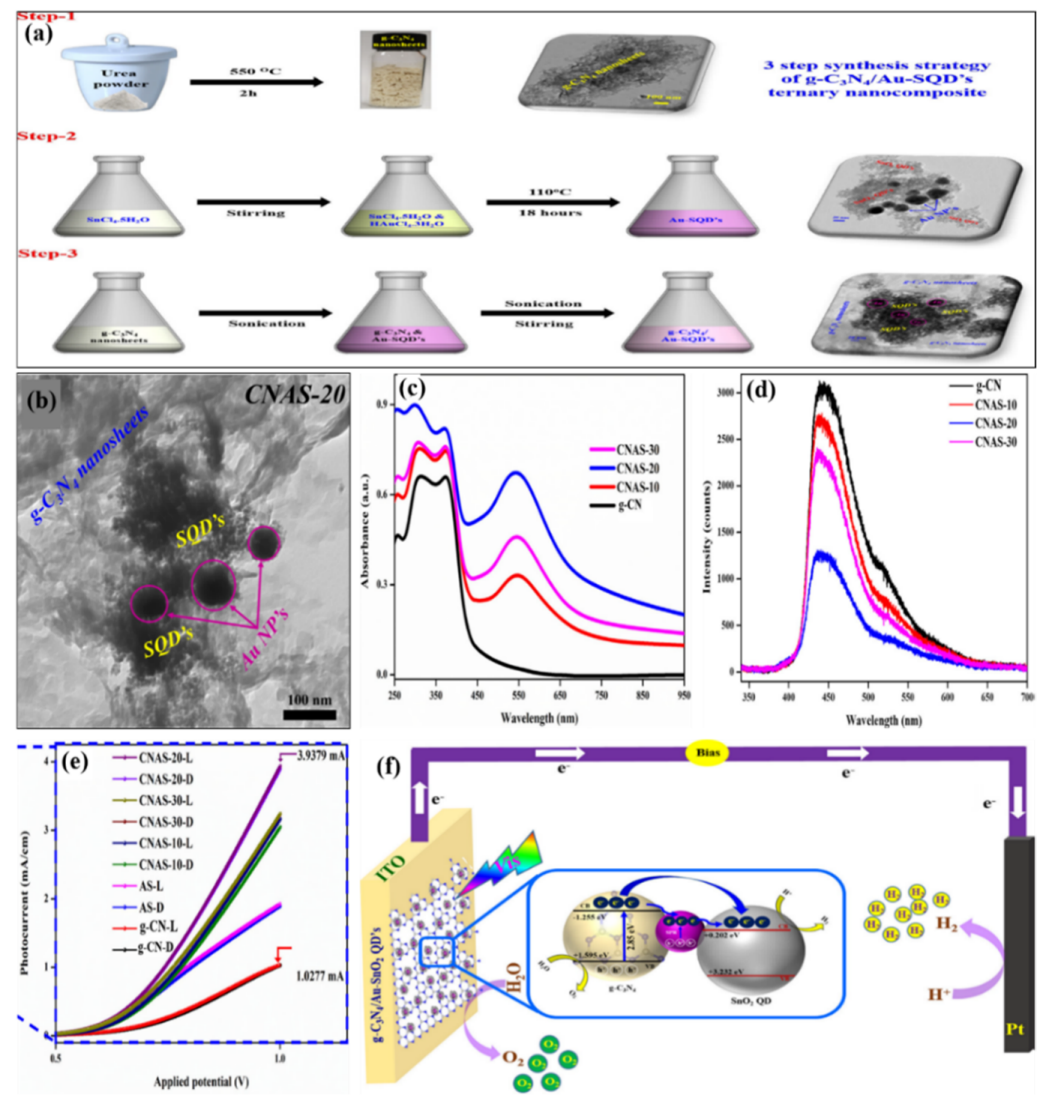
Figure 7. (**a**) Formation mechanism of CN/Au-SQD ternary heterostructured material, (**b**) TEM image of CN/Au-SQD heterostructured material, (**c**) optical absorption spectra, (**d**) PL spectra, (**e**) LSV curves, and (**f**) charge transfer mechanism of the CN/Au-SQD ternary heterostructured electrodes. Reprinted with permission from reference [96], Copyright 2020, Elsevier.

Li and co-workers systematically fabricated 0D Bi_2O_3 NPs encapsulated with $BiPO_4$ nanorods that were distributed over the surface of $g-C_3N_4$, which formed the CN/BO/BP ternary heterostructured electrode using the facile hydrothermal method followed by calcination process [97]. The XRD results demonstrated that the ternary CN/BO/BP heterostructured electrode exhibited $g-C_3N_4$, Bi_2O_3, and $BiPO_4$ phases, confirming the presence of individual components. The morphology results showed that the Bi_2O_3 NPs were anchored over $BiPO_4$ nanorods, and the binary BO/BP heterostructured material was distributed over the surface of the $g-C_3N_4$ nanosheets. When compared to pure samples, the light absorption efficiency of the CN/BO/BP heterostructured electrode enhanced towards the visible region. From the EIS analysis, the ternary CN/BO/BP photoanode exhibited the lowest R_{ct} value compared to the pure CN, BO, BP, CN/BP, BO/BP electrodes. From the LSV results, the CN/BO/BP photoanode showed a photocurrent density of 0.095 mA cm^{-2} at 1.25 V vs. Ag/AgCl in 0.1 M Na_2SO_4 electrolyte under solar light irradiation, and the value was 2.4 and 1.3 times superior to the BP and BO/BP electrodes, respectively. This enhanced PEC performance could be ascribed to the formation of the interfacial heterostructure with the Z-scheme process, which hinders the recombination of charge carriers and higher solar-light absorption ability.

Chaudhary et al. have developed a novel ternary heterostructured electrode consisting of the TiO_2 NPs with carbon nanotubes that dispersed over the g-C_3N_4 nanosheets (TO/CN/CNT) using a facile hydrothermal method [98]. The XRD results (Figure 8a) confirmed the anatase phase of TiO_2, the graphitic nature of CNT, and the interlayer stacking of CN. The morphology results (Figure 8b) displayed that the TiO_2 NPs and CNTs were decorated on the surface of CN nanosheets. Further, the TO/CN/CNT ternary heterostructured electrode showed an enlarged light-harvesting performance. The R_{ct} value (Figure 8c) of the TO/CN/CNT ternary heterostructured electrode was significantly reduced compared to the TO, CN, and TO/CN electrodes under visible-light illumination. The photocurrent density (Figure 8d) of the TO/CN/CNT ternary electrode showed 2.43 mA cm^{-2} at 0.6 V vs. Ag/AgCl in 0.5 M Na_2SO_4 electrolyte under visible-light, and the current density value was around 6.4, and 3.2 times higher than the CN, TO/CN photoelectrodes, respectively. Thus, the formation of interfacial interactions among the three components (Figure 8e) could effectively improve the migration of charge carriers with more separation, which in turn enhanced the PEC water splitting efficiency.

Si and co-workers systematically fabricated graphdiyne (GDY)-anchored g-C_3N_4/NiFe-layered double hydroxide (CN/GDY/NF) electrode via the facile hydrothermal method [99]. The XRD results revealed that CN, GDY, and NF crystal phases were presented in the CN/GDY/NF heterostructured electrode without any impurity phases. Further, the FTIR and XPS results confirmed that the heterostructured material consisted of individual compounds. The CN/GDY/NF heterostructured material presented a higher specific surface area of 208.75 m^2 g^{-1} than the pure CN (126.32 m^2 g^{-1}), GDY (95.03 m^2 g^{-1}), and NF (42.63 m^2 g^{-1}) materials. The visible-light-harvesting ability was significantly enhanced after forming the CN/GDY/NF heterostructured electrode, and the PL intensity was diminished compared to the pristine CN, GDY, and NF samples. From the EIS results, the CN/GDY/NF photoelectrode showed the lowest R_{ct} value than the pure CN, GDY, and NF electrodes. Furthermore, the photocurrent density of ternary CN/GDY/NF photoelectrode was observed around 0.178 mA cm^{-2} at 1.4 V vs. RHE under visible light, and the photocurrent density value was around 45 times higher than the pristine CN electrode. The enhanced water splitting activity was ascribed to the formation of synergistic interactions among the ternary components, which emphasized the visible-light absorption ability and quick transfer of charge carriers with lower charge-transfer resistance.

Gopalakrishnan et al. adopted the spin-coating technique and successfully fabricated the heterostructured electrode in which $SrTiO_3$ NPs covered on the surface of g-C_3N_4 nanosheets and coupled with silicon nanowires (ST/CN/Si) [100]. The crystallographic analysis confirmed the formation of ST, CN, and Si phases in the ST/CN/Si heterostructured electrode without any impurity phases. The morphology results demonstrated the uniform distribution of ST nanoparticles and Si nanowires on the surface of g-C_3N_4, which confirmed the formation of a synergistic interfacial heterostructure. Further, the light-harvesting ability was significantly enhanced towards the visible region through the formation of a ternary ST/CN/Si heterostructured electrode. From the EIS analysis, the ST/CN/Si photocathode exhibited the lowest charge transfer resistance than the pure CN, ST, Si, and CN@Si electrodes. The photocurrent density of the ST/CN/Si heterostructured electrode showed around 28 mA cm^{-2} at 0.8 V vs. RHE in 0.5 M Na_2SO_4 electrolyte under visible light, and this current density value was superior to the other electrodes. Therefore, the introduction of Si nanowires and ST nanoparticles on the surface of CN considerably enriched the light-harvesting ability, separation of e$^-$/h$^+$ pairs, and quicker interfacial charge transfer, which significantly progressed the water-splitting ability.
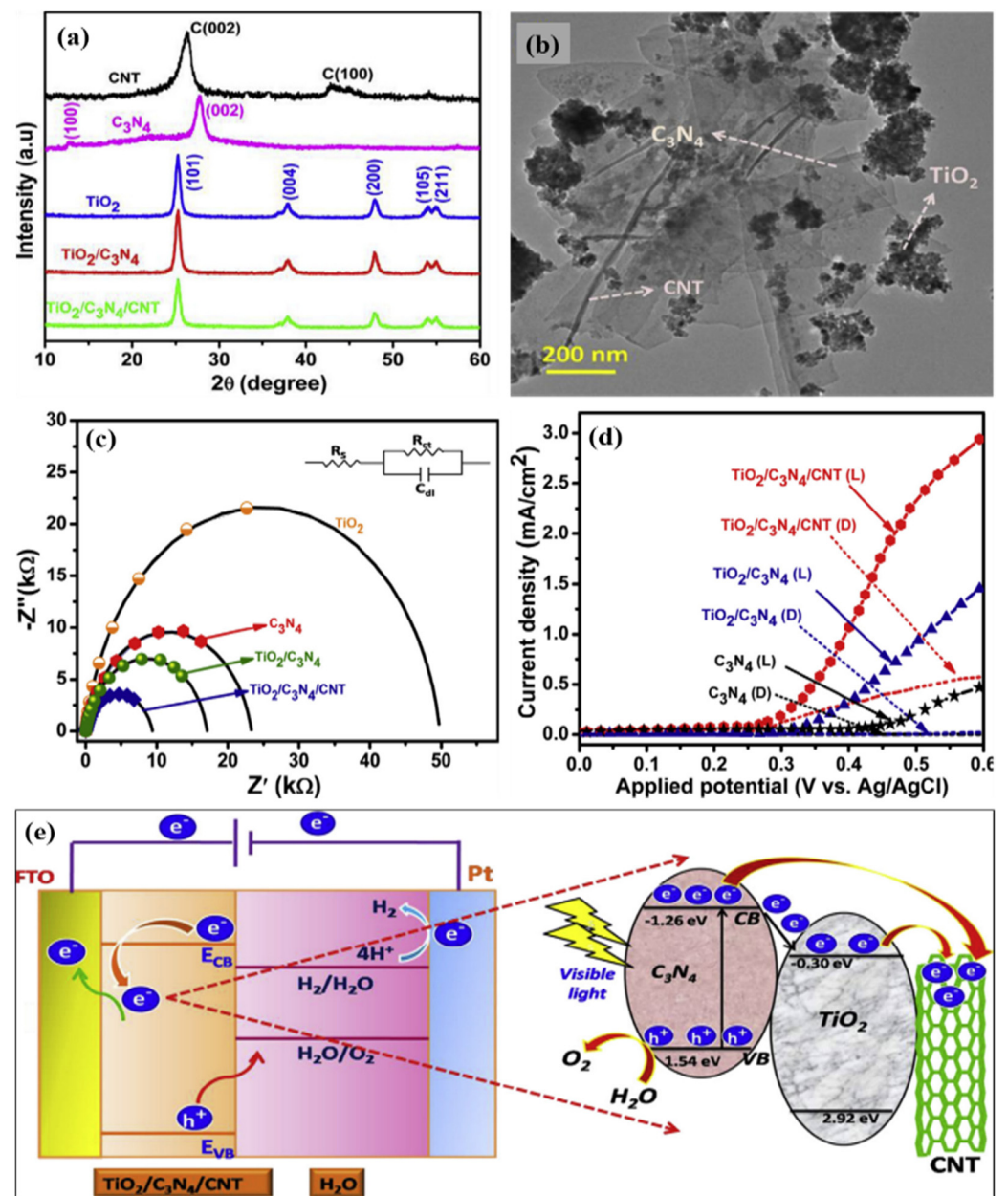
Figure 8. (**a**) XRD patterns, (**b**) TEM image of TO/CN/CNT heterostructured material, (**c**) Nyquist plots, (**d**) LSV curves, and (**e**) charge transfer mechanism of the TO/CN/CNT ternary heterostructured electrode. Reprinted with permission from reference [98], Copyright 2020, Elsevier.

To enhance the utility of visible-light and diminish the reunion of charge carriers, a novel fluorine-doped, chlorine-intercalated g-C_3N_4 combined with various concentrations of BiOI (10, 25, 57, and 75%)-based CNF-Cl/BI heterostructured electrodes was prepared using a facile in-situ hydrothermal technique by Alam and co-workers [101]. The XRD results confirmed the interlayer stacking of the CN units and the tetragonal phase of BI even after the formation of a CNF-Cl/BI heterostructure. The morphology results demonstrated that the BI nanoplates were uniformly covered on the surface of the CNF-Cl electrode. The bandgap tuning was observed for the CNF-Cl/BI heterostructured electrode when compared to pure samples, which significantly enhanced the visible-light absorption ability. From the EIS results, the CNF-Cl/BI50% heterostructured electrode exhibited the lowest R_{ct} value than the remaining samples. Moreover, the photocurrent density of CNF-Cl/BI50% photoanode was observed around 1.28 mA cm^{-2} at 1.23 V vs. RHE under visible-light illumination, and the value was around 4.6 and 3.2 times higher than the CNF-Cl and BI

electrodes, respectively. Thus, the formation of synergistic interfaces, improved charge separation, and the enlarged light-harvesting ability significantly enhanced the PEC water-splitting performance.

Wu et al. systematically fabricated a novel Bi_2MoO_6-Ru binary heterostructured material anchored on the surface of g-C_3N_4 (BMO/Ru/CN) using a facile hydrothermal method (Figure 9a) [102]. The XRD results (Figure 9b) demonstrated that all the crystal phases of BMO, Ru, and CN were presented in the BMO/Ru/CN heterostructured electrode without any impurity phases. Further, the peak shift of XPS confirmed the formation of ternary BMO/Ru/CN heterostructured material. The visible-light-harvesting ability (Figure 9c) was significantly enhanced after the BMO/Ru/CN heterostructure formation, and the PL intensity was diminished compared to the BMO, CN, BMO/Ru, Ru/CN, and BMO/CN samples. The morphology results (Figure 9d and e) revealed the uniform distribution of BMO microspheres and Ru NPs on the surface of CN. From the EIS results (Figure 9f), the BMO/Ru/CN heterostructured electrode showed the lowest R_{ct} value than the BMO, CN, BMO/Ru, Ru/CN, and BMO/CN electrodes. Furthermore, the photocurrent density of ternary BMO/Ru/CN photoelectrode was around 1.0 mA cm^{-2} at 1.4 V vs. Ag/AgCl under visible light, and the obtained photocurrent density was approximately 25 times higher than the BMO/CN electrode. The enhanced water splitting performance (Figure 9g) was ascribed to the formation of synergistic coupling among the ternary components, which emphasized the visible-light absorption ability and facile transportation of charge carriers with a lower R_{ct} value.

Patnaik and colleagues successfully synthesized the various concentrations (2, 4, 6, and 8 wt.%) of Cu-promoted MoO_3/g-C_3N_4 (Cu/MO/CN) hybrid heterostructured electrode using the in-situ pyrolysis followed by the impregnation techniques [103]. The XRD results confirmed that the interlayer stacking of the CN units, the orthorhombic phase of MoO_3, and the heterostructure formation did not influence the individual phase. The morphological investigation inferred that the irregular-shaped MoO_3 nanocrystals and Cu nanoparticles dispersed on the g-C_3N_4 surface. Further, the visible-light absorption ability was improved by forming the heterostructure, and the distribution of Cu NPs was confirmed by the occurrence of a surface plasmon resonance band. From the EIS results, the 2% Cu/MO/CN heterostructured electrode exhibited the lowest charge-transfer resistance value among other samples. Further, the 2% Cu/MO/CN heterostructured electrode showed a photocurrent density of around 5.1 mA cm^{-2} using 0.5 M Na_2SO_4 electrolyte under visible-light illumination, which was higher than the other electrodes. Thus, the synergistic interactions having rich-oxygen vacancies could effectively improve the mobility of charge carriers and diminish the reunion of electron/hole pairs, which enhanced the PEC performance. The PEC performance of g-C_3N_4-based various ternary heterostructured electrodes is presented in Table 2.
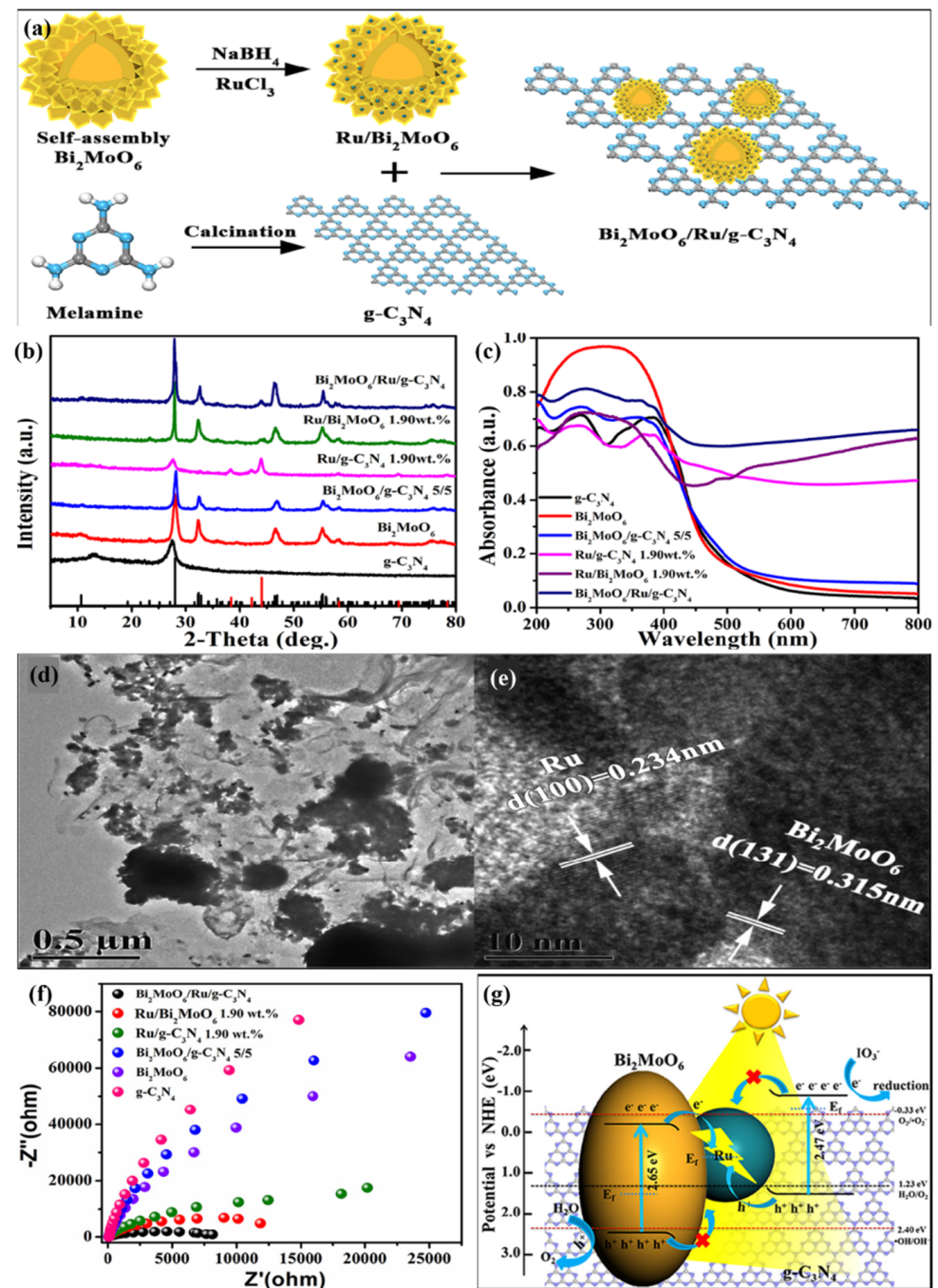
Figure 9. (**a**) Formation mechanism of the BO/Ru/CN ternary heterostructured material, (**b**) XRD patterns, (**c**) optical absorption spectra, (**d**) TEM image, (**e**) HRTEM image of BO/Ru/CN heterostructured material, (**f**) Nyquist plots, and (**g**) charge transfer mechanism of the BO/Ru/CN ternary heterostructured electrode. Reprinted with permission from reference [102], Copyright 2019, American Chemical Society.

Table 2. The PEC performance of g-C$_3$N$_4$-based ternary heterostructured photoelectrodes.

Photoelectrodes	Synthesis Methods	Potential (V)	Electrolytes	Light Sources	Photocurrent Density (mA cm^{-2})	Ref.
ZnO/Au/g-C$_3$N$_4$	Thermal vapor condensation	−0.5 vs. RHE	0.2 M Na$_2$SO$_4$	Solar	−0.29	[104]
g-C$_3$N$_4$/Pt/ZnO	Spin coating	0.5 vs. Ag/AgCl	0.5 M Na$_2$SO$_4$	Solar	0.12	[105]

Table 2. *Cont.*

Photoelectrodes	Synthesis Methods	Potential (V)	Electrolytes	Light Sources	Photocurrent Density (mA cm^{-2})	Ref.
g-C$_3$N$_4$/Ti-Fe$_2$O$_3$	Electrodeposition	0.23 vs. Ag/AgCl	1.0 M NaOH	Visible	2.55	[106]
g-C$_3$N$_4$/TiN-NFG	Ultra-sonication	0.11 vs. RHE	0.5 M Na$_2$SO$_4$	Solar	−0.196	[107]
TiO$_2$@g-C$_3$N$_4$/Co-Pi	Hydrothermal, chemical bath deposition, electrodeposition	1.23 vs. RHE	0.1 M Na$_2$SO$_4$	Solar	1.6	[108]
Ag@g-C$_3$N$_4$/ZnS	electrophoretic deposition	1.23 vs. RHE	0.3 M KCl	Visible	0.1	[109]
Fluorine-dopedg-C$_3$N$_4$/TiO$_2$	In-situ growth	0.6 vs. Ag/AgCl	0.1 M KOH	Visible	0.18	[110]
Ti^{3+}-TiO$_2$/O-g-C$_3$N$_4$	Hydrothermal	0.1 vs. Ag/AgCl	0.1 M Na$_2$SO$_4$	Visible	0.0034	[111]
TiO$_2$@P-C$_3$N$_4$/Co$_3$O$_4$	Chemical bath deposition	1.23 vs. RHE	0.5 M Na$_2$SO$_4$	Visible	1.58	[112]
NiFe/N-rGO/g-C$_3$N$_4$	Calcinations, electrostatic self-assembly, and hydrothermal	0.8 vs. Ag/AgCl	0.1 M Na$_2$SO$_4$	Visible	−0.97	[113]

5. Future Perspectives

The experimental evidence revealed that g-C$_3$N$_4$-could be used as a photocatalyst and decent catalyst support material for various metal oxide-based heterostructured electrodes fabrication [29,114]. However, hybridizing the g-C$_3$N$_4$ with a second carbon component could further enhance the overall conductivity of the heterostructured electrodes and the durability of g-C$_3$N$_4$ catalysts [40,52,115]. Thus far, experimental investigations indicated that g-C$_3$N$_4$-carbon hybrid catalysts could improve the overall PEC performance.

(i)   To further improve the photocatalytic activity and water splitting efficiency, innovative strategies are required to synthesize g-C$_3$N$_4$-based heterostructured electrodes with various hierarchical and porous morphologies [70,91,116].

(ii) Most of the reported heterostructured catalysts have been investigated using g-C$_3$N$_4$ nanosheet morphologies only. It is worth exploring other morphologies of g-C$_3$N$_4$ such as nanorods, nanoparticles, nanotubes, porous nanosheets, etc. [61,64].

(iii) The simultaneous modification of g-C$_3$N$_4$-based heterostructured electrodes through one or more of the following methods: (i) the rational design of nanoarrays architectures, (ii) doping of atoms or molecules, and (iii) loading of various co-catalysts. These strategies can also offer extraordinary improvement of PEC performance due to the synergetic effect of the different catalytic mechanisms [63,117].

(iv) Moreover, the theoretical and computational screening investigations must be performed to elucidate the charge transfer mechanism, PEC water splitting efficiency, stability, and strategies for improving the overall photocatalytic activity of g-C$_3$N$_4$-based catalysts.

(v)   In addition, these computational studies can serve as a guide for experimentalists, especially for selecting the optimal materials and making their hybrid compositions. Therefore, understanding the effect of materials matrices on water splitting performance is needed. It will also help to develop the other requirements of catalysts, such as stability and cost consumption for the real-time application of the PEC water splitting process.

(vi) Furthermore, electrolytes used in the PEC water splitting have significant influences on the overall PEC performance. Besides, it is also essential to maintain the system at a constant temperature to get accurate PEC measurements. Therefore, it is suggested to utilize water baths or thermostatic systems during the PEC measurements. In addition, a light source should also be equipped with infrared cut-off filters to block the unnecessary heating effect and the evaporation of electrolytes.

6. Conclusions

This review summarized and discussed the recent advances in g-C$_3$N$_4$-based binary and ternary heterostructured electrodes for PEC water splitting. The PEC water splitting is the most straightforward and promising way to produce solar fuels, considering the

safety factor, environmental friendliness, and the abundance of solar energy. The process is usually carried out at room temperature and the usage of inorganic materials, lending the system robustness, which is difficult to achieve with organic-based photocatalytic materials. The g-C_3N_4-based binary and ternary heterostructured electrodes exhibit excellent water splitting performance and stability due to the synergistic interactions with large surface area and facile transportation of charge carriers. There are certain drawbacks associated with PEC water splitting; however, they can be overcome by combining it with the biological processes that are capable of producing a large quantity of hydrogen. The heterostructured electrodes made of g-C_3N_4 with various binary and ternary semiconductor nanostructured materials are promising photocatalysts in terms of efficient formation of reactive oxygen species and lower recombination of electrons and holes. From the results mentioned above, the ternary g-C_3N_4-based heterostructured electrodes exhibited superior photocurrent densities with lower R_{ct} value and enlarged visible-light absorption capability when compared to the binary g-C_3N_4-based heterostructured electrodes. This phenomenon could be attributed to the large surface area, synergistic interfaces among the ternary components with a quick charge carrier transportation, thus eventually reducing the reunion of charge carriers. Apart from the experiments discussed here, the g-C_3N_4-based heterostructured electrodes can also be used in various concentrations of different electrolytes with a wide range of operating potentials. Experimental studies have revealed that g-C_3N_4-based heterostructured electrodes could act as efficient photocatalyst support materials for PEC water splitting. However, several bottlenecks still exist that can hinder the use of g-C_3N_4 for the PEC water splitting reactions, which needs further elaborative research on this fascinating material and the other g-C_3N_4-based heterostructured electrode designs.

Author Contributions: Conceptualization and methodology, writing—original draft preparation, R.K.; writing—original draft preparation, S.G.P.; writing—editing, T.G.L.; writing—editing, C.R.M.; writing—editing, D.-Y.L.; resources, J.S.; funding acquisition, writing—review and editing, S.K.B. All authors have read and agreed to the published version of the manuscript.

Conflicts of Interest: The authors declare that they have no known competing financial interests or personal relationships that could have appeared to influence the work reported in this paper.

References

1. Siavash Moakhar, R.; Hosseini-Hosseinabad, S.M.; Masudy-Panah, S.; Seza, A.; Jalali, M.; Fallah-Arani, H.; Dabir, F.; Gholipour, S.; Abdi, Y.; Bagheri-Hariri, M.; et al. Photoelectrochemical water-splitting using CuO-based electrodes for hydrogen production: A review. *Adv. Mater.* **2021**, *33*, 2007285. [CrossRef] [PubMed]
2. Yu, J.M.; Lee, J.; Kim, Y.S.; Song, J.; Oh, J.; Lee, S.M.; Jeong, M.; Kim, Y.; Kwak, J.H.; Cho, S.; et al. High-performance and stable photoelectrochemical water splitting cell with organic-photoactive-layer-based photoanode. *Nat. Commun.* **2020**, *11*, 5509. [CrossRef] [PubMed]
3. Hamdani, I.R.; Bhaskarwar, A.N. Recent progress in material selection and device designs for photoelectrochemical water-splitting. *Renew. Sustain. Energy Rev.* **2021**, *138*, 110503. [CrossRef]
4. Cen, J.; Wu, Q.; Liu, M.; Orlov, A. Developing new understanding of photoelectrochemical water splitting via in-situ techniques: A review on recent progress. *Green Energy Environ.* **2017**, *2*, 100–111. [CrossRef]
5. Joy, J.; Mathew, J.; George, S.C. Nanomaterials for photoelectrochemical water splitting—Review. *Int. J. Hydrogen Energy* **2018**, *43*, 4804–4817. [CrossRef]
6. Yang, W.; Park, J.; Kwon, H.-C.; Hutter, O.S.; Phillips, L.J.; Tan, J.; Lee, H.; Lee, J.; Tilley, S.D.; Major, J.D.; et al. Solar water splitting exceeding 10% efficiency via low-cost Sb_2Se_3 photocathodes coupled with semitransparent perovskite photovoltaics. *Energy Environ. Sci.* **2020**, *13*, 4362–4370. [CrossRef]
7. Nadeem, M.A.; Khan, M.A.; Ziani, A.A.; Idriss, H. An overview of the photocatalytic water splitting over suspended particles. *Catalysts* **2021**, *11*, 60. [CrossRef]
8. Varadhan, P.; Fu, H.-C.; Kao, Y.-C.; Horng, R.-H.; He, J.-H. An efficient and stable photoelectrochemical system with 9% solar-to-hydrogen conversion efficiency via InGaP/GaAs double junction. *Nat. Commun.* **2019**, *10*, 5282. [CrossRef] [PubMed]
9. Fernández-Climent, R.; Giménez, S.; García-Tecedor, M. The role of oxygen vacancies in water splitting photoanodes. *Sustain. Energy Fuels* **2020**, *4*, 5916–5926. [CrossRef]

10. Elbakkay, M.H.; El Rouby, W.M.A.; El-Dek, S.I.; Farghali, A.A. S-TiO$_2$/S-reduced graphene oxide for enhanced photoelectrochemical water splitting. *Appl. Surf. Sci.* **2018**, *439*, 1088–1102. [CrossRef]

11. Jian, J.; Sun, J. A review of recent progress on silicon carbide for photoelectrochemical water splitting. *Solar RRL* **2020**, *4*, 2000111. [CrossRef]

12. Zheng, G.; Wang, J.; Liu, H.; Murugadoss, V.; Zu, G.; Che, H.; Lai, C.; Li, H.; Ding, T.; Gao, Q.; et al. Tungsten oxide nanostructures and nanocomposites for photoelectrochemical water splitting. *Nanoscale* **2019**, *11*, 18968–18994. [CrossRef] [PubMed]

13. Jin, S. What else can photoelectrochemical solar energy conversion do besides water splitting and CO$_2$ reduction? *ACS Energy Lett.* **2018**, *3*, 2610–2612. [CrossRef]

14. Wang, S.; Lu, A.; Zhong, C.-J. Hydrogen production from water electrolysis: Role of catalysts. *Nano Converg.* **2021**, *8*, 4. [CrossRef] [PubMed]

15. Ke, J.; He, F.; Wu, H.; Lyu, S.; Liu, J.; Yang, B.; Li, Z.; Zhang, Q.; Chen, J.; Lei, L.; et al. Nanocarbon-enhanced 2D photoelectrodes: A new paradigm in photoelectrochemical water splitting. *Nanomicro Lett.* **2020**, *13*, 24. [CrossRef] [PubMed]

16. Niu, F.; Wang, D.; Li, F.; Liu, Y.; Shen, S.; Meyer, T.J. Hybrid photoelectrochemical water splitting systems: From interface design to system assembly. *Adv. Energy Mater.* **2020**, *10*, 1900399. [CrossRef]

17. Ye, K.-H.; Li, H.; Huang, D.; Xiao, S.; Qiu, W.; Li, M.; Hu, Y.; Mai, W.; Ji, H.; Yang, S. Enhancing photoelectrochemical water splitting by combining work function tuning and heterojunction engineering. *Nat. Commun.* **2019**, *10*, 3687. [CrossRef] [PubMed]

18. Ali, M.; Pervaiz, E.; Noor, T.; Rabi, O.; Zahra, R.; Yang, M. Recent advancements in MOF-based catalysts for applications in electrochemical and photoelectrochemical water splitting: A review. *Int. J. Energy Res.* **2021**, *45*, 1190–1226. [CrossRef]

19. Tan, H.L.; Abdi, F.F.; Ng, Y.H. Heterogeneous photocatalysts: An overview of classic and modern approaches for optical, electronic, and charge dynamics evaluation. *Chem. Soc. Rev.* **2019**, *48*, 1255–1271. [CrossRef]

20. Franchi, D.; Amara, Z. Applications of sensitized semiconductors as heterogeneous visible-light photocatalysts in organic synthesis. *ACS Sustain. Chem. Eng.* **2020**, *8*, 15405–15429. [CrossRef]

21. Arunachalam, P.; Nagai, K.; Amer, M.S.; Ghanem, M.A.; Ramalingam, R.J.; Al-Mayouf, A.M. Recent developments in the use of heterogeneous semiconductor photocatalyst based materials for a visible-light-induced water-splitting system—A brief review. *Catalysts* **2021**, *11*, 160. [CrossRef]

22. Tang, P.; Arbiol, J. Engineering surface states of hematite based photoanodes for boosting photoelectrochemical water splitting. *Nanoscale Horiz.* **2019**, *4*, 1256–1276. [CrossRef]

23. Wu, Y.; Bi, L. Research progress on catalytic water splitting based on polyoxometalate/semiconductor composites. *Catalysts* **2021**, *11*, 524. [CrossRef]

24. Ng, B.-J.; Putri, L.K.; Kong, X.Y.; Teh, Y.W.; Pasbakhsh, P.; Chai, S.-P. Z-scheme photocatalytic systems for solar water splitting. *Adv. Sci.* **2020**, *7*, 1903171. [CrossRef]

25. Zou, X.; Sun, Z.; Hu, Y.H. g-C$_3$N$_4$-based photoelectrodes for photoelectrochemical water splitting: A review. *J. Mater. Chem. A* **2020**, *8*, 21474–21502. [CrossRef]

26. Daulbayev, C.; Sultanov, F.; Bakbolat, B.; Daulbayev, O. 0D, 1D and 2D nanomaterials for visible photoelectrochemical water splitting-A Review. *Int. J. Hydrogen Energy* **2020**, *45*, 33325–33342. [CrossRef]

27. Mishra, A.; Mehta, A.; Basu, S.; Shetti, N.P.; Reddy, K.R.; Aminabhavi, T.M. Graphitic carbon nitride (g–C3N4)–based metal-free photocatalysts for water splitting: A review. *Carbon* **2019**, *149*, 693–721. [CrossRef]

28. Safaei, J.; Mohamed, N.A.; Mohamad Noh, M.F.; Soh, M.F.; Ludin, N.A.; Ibrahim, M.A.; Roslam Wan Isahak, W.N.; Mat Teridi, M.A. Graphitic carbon nitride (g-C$_3$N$_4$) electrodes for energy conversion and storage: A review on photoelectrochemical water splitting, solar cells and supercapacitors. *J. Mater. Chem. A* **2018**, *6*, 22346–22380. [CrossRef]

29. Wang, L.; Si, W.; Tong, Y.; Hou, F.; Pergolesi, D.; Hou, J.; Lippert, T.; Dou, S.X.; Liang, J. Graphitic carbon nitride (g-C$_3$N$_4$)-based nanosized heteroarrays: Promising materials for photoelectrochemical water splitting. *Carbon Energy* **2020**, *2*, 223–250. [CrossRef]

30. Wang, S.; Zhang, J.; Li, B.; Sun, H.; Wang, S. Engineered graphitic carbon nitride-based photocatalysts for visible-light-driven water splitting: A review. *Energy Fuel* **2021**, *35*, 6504–6526. [CrossRef]

31. Kumar, D.; Sharma, S.; Khare, N. Enhanced photoelectrochemical performance of NaNbO$_3$ nanofiber photoanodes coupled with visible light active g-C$_3$N$_4$ nanosheets for water splitting. *Nanotechnology* **2020**, *31*, 135402. [CrossRef] [PubMed]

32. Acharya, R.; Parida, K. A review on TiO$_2$/g-C$_3$N$_4$ visible-light-responsive photocatalysts for sustainable energy generation and environmental remediation. *J. Environ. Chem. Eng.* **2020**, *8*, 103896. [CrossRef]

33. Asadzadeh-Khaneghah, S.; Habibi-Yangjeh, A. g-C$_3$N$_4$/carbon dot-based nanocomposites serve as efficacious photocatalysts for environmental purification and energy generation: A review. *J. Clean. Prod.* **2020**, *276*, 124319. [CrossRef]

34. Ong, W.-J.; Tan, L.-L.; Ng, Y.H.; Yong, S.-T.; Chai, S.-P. Graphitic carbon nitride (g-C$_3$N$_4$)-based photocatalysts for artificial photosynthesis and environmental remediation: Are we a step closer to achieving sustainability? *Chem. Rev.* **2016**, *116*, 7159–7329. [CrossRef] [PubMed]

35. Ren, Y.; Zeng, D.; Ong, W.-J. Interfacial engineering of graphitic carbon nitride (g-C$_3$N$_4$)-based metal sulfide heterojunction photocatalysts for energy conversion: A review. *Chin. J. Catal.* **2019**, *40*, 289–319. [CrossRef]

36. Kumar, P.; Boukherroub, R.; Shankar, K. Sunlight-driven water-splitting using two-dimensional carbon based semiconductors. *J. Mater. Chem. A* **2018**, *6*, 12876–12931. [CrossRef]

37. Reddy, A.S.; Kim, J. An efficient g-C$_3$N$_4$-decorated CdS-nanoparticle-doped Fe$_3$O$_4$ hybrid catalyst for an enhanced H$_2$ evolution through photoelectrochemical water splitting. *Appl. Surf. Sci.* **2020**, *513*, 145836. [CrossRef]

38. Ong, W.-J. 2D/2D graphic carbon nitride (g-C$_3$N$_4$) heterojunction nanocomposites for photocatalysis: Why does face-to-face interface matter? *Front. Mater.* **2017**, *4*, 11. [CrossRef]

39. Zhu, B.; Zhang, L.; Cheng, B.; Yu, J. First-principle calculation study of tri-s-triazine-based g-C$_3$N$_4$: A review. *Appl. Catal. B* **2018**, *224*, 983–999. [CrossRef]

40. Hosseini H., S.M.; Siavash Moakhar, R.; Soleimani, F.; Sadrnezhaad, S.K.; Masudy-Panah, S.; Katal, R.; Seza, A.; Ghane, N.; Ramakrishna, S. One-pot microwave synthesis of hierarchical C-doped CuO dandelions/g-C$_3$N$_4$ nanocomposite with enhanced photostability for photoelectrochemical water splitting. *Appl. Surf. Sci.* **2020**, *530*, 147271. [CrossRef]

41. Ismael, M. A review on graphic carbon nitride (g-C$_3$N$_4$) based nanocomposites: Synthesis, categories, and their application in photocatalysis. *J. Alloys Compd.* **2020**, *846*, 156446. [CrossRef]

42. Tamirat, A.G.; Rick, J.; Dubale, A.A.; Su, W.-N.; Hwang, B.-J. Using hematite for photoelectrochemical water splitting: A review of current progress and challenges. *Nanoscale Horiz.* **2016**, *1*, 243–267. [CrossRef] [PubMed]

43. Wang, F.; Li, Q.; Xu, D. Recent progress in semiconductor-based nanocomposite photocatalysts for solar-to-chemical energy conversion. *Adv. Energy Mater.* **2017**, *7*, 1700529. [CrossRef]

44. Lui, Y.H.; Zhang, B.; Hu, S. Rational design of photoelectrodes for photoelectrochemical water splitting and CO$_2$ reduction. *Front. Phys.* **2019**, *14*, 53402. [CrossRef]

45. Chen, S.; Huang, D.; Xu, P.; Xue, W.; Lei, L.; Cheng, M.; Wang, R.; Liu, X.; Deng, R. Semiconductor-based photocatalysts for photocatalytic and photoelectrochemical water splitting: Will we stop with photocorrosion? *J. Mater. Chem. A* **2020**, *8*, 2286–2322. [CrossRef]

46. Sumesh, C.K.; Peter, S.C. Two-dimensional semiconductor transition metal based chalcogenide based heterostructures for water splitting applications. *Dalton Trans.* **2019**, *48*, 12772–12802. [CrossRef] [PubMed]

47. Serpone, N.; Emeline, A.V.; Ryabchuk, V.K.; Kuznetsov, V.N.; Artem'ev, Y.M.; Horikoshi, S. Why do hydrogen and oxygen yields from semiconductor-based photocatalyzed water splitting remain disappointingly low? Intrinsic and extrinsic factors impacting surface redox reactions. *ACS Energy Lett.* **2016**, *1*, 931–948. [CrossRef]

48. Gupta, N.M. Factors affecting the efficiency of a water splitting photocatalyst: A perspective. *Renew. Sustain. Energy Rev.* **2017**, *71*, 585–601. [CrossRef]

49. Mahzoon, S.; Nowee, S.M.; Haghighi, M. Synergetic combination of 1D-2D g-C$_3$N$_4$ heterojunction nanophotocatalyst for hydrogen production via water splitting under visible light irradiation. *Renew. Energy* **2018**, *127*, 433–443. [CrossRef]

50. Wang, H.; Li, X.; Yang, J. The g-C$_3$N$_4$/C$_2$N nanocomposite: A g-C$_3$N$_4$-based water-splitting photocatalyst with enhanced energy efficiency. *ChemPhysChem* **2016**, *17*, 2100–2104. [CrossRef]

51. Yang, X.; Singh, D.; Ahuja, R. Recent advancements and future prospects in ultrathin 2D semiconductor-based photocatalysts for water splitting. *Catalysts* **2020**, *10*, 1111. [CrossRef]

52. Yousefzadeh, S.; Fathi, B. Construction of carbon nanotube-g-C$_3$N$_4$ nanocomposite photoanode for the enhanced photoelectrochemical activity in water splitting. *J. Electroanal. Chem.* **2020**, *878*, 114580. [CrossRef]

53. Patnaik, S.; Sahoo, D.P.; Parida, K. An overview on Ag modified g-C$_3$N$_4$ based nanostructured materials for energy and environmental applications. *Renew. Sustain. Energy Rev.* **2018**, *82*, 1297–1312. [CrossRef]

54. Sepahvand, H.; Sharifnia, S. Photocatalytic overall water splitting by Z-scheme g-C$_3$N$_4$/BiFeO$_3$ heterojunction. *Int. J. Hydrogen Energy* **2019**, *44*, 23658–23668. [CrossRef]

55. Yang, Y.; Wang, S.; Li, Y.; Wang, J.; Wang, L. Strategies for efficient solar water splitting using carbon nitride. *Chem. Asian J.* **2017**, *12*, 1421–1434. [CrossRef]

56. Gandamalla, A.; Manchala, S.; Anand, P.; Fu, Y.-P.; Shanker, V. Development of versatile CdMoO$_4$/g-C$_3$N$_4$ nanocomposite for enhanced photoelectrochemical oxygen evolution reaction and photocatalytic dye degradation applications. *Mat. Today Chem.* **2021**, *19*, 100392. [CrossRef]

57. Paul, A.M.; Sajeev, A.; Nivetha, R.; Gothandapani, K.; Bhardwaj, P.; Govardhan, K.; Raghavan, V.; Jacob, G.; Sellapan, R.; Jeong, S.K.; et al. Cuprous oxide (Cu$_2$O)/graphitic carbon nitride (g-C$_3$N$_4$) nanocomposites for electrocatalytic hydrogen evolution reaction. *Diam. Relat. Mater.* **2020**, *107*, 107899. [CrossRef]

58. Fu, J.; Yu, J.; Jiang, C.; Cheng, B. g-C$_3$N$_4$-based heterostructured photocatalysts. *Adv. Energy Mater.* **2018**, *8*, 1701503. [CrossRef]

59. Zhang, L.; Zhang, M.; Song, X.; Wang, H.; Bian, Z. One-step synthesis of MnOx/g-C$_3$N$_4$ nanocomposites for enhancing the visible light photoelectrochemical oxidation performance. *Chem. Eng. J.* **2020**, *399*, 125825. [CrossRef]

60. Wang, J.; Yang, Z.; Gao, X.; Yao, W.; Wei, W.; Chen, X.; Zong, R.; Zhu, Y. Core-shell g-C$_3$N$_4$@ZnO composites as photoanodes with double synergistic effects for enhanced visible-light photoelectrocatalytic activities. *Appl. Catal. B* **2017**, *217*, 169–180. [CrossRef]

61. Xiao, L.; Liu, T.; Zhang, M.; Li, Q.; Yang, J. Interfacial construction of zero-dimensional/one-dimensional g-C$_3$N$_4$ nanoparticles/TiO$_2$ nanotube arrays with Z-scheme heterostructure for improved photoelectrochemical water splitting. *ACS Sustain. Chem. Eng.* **2019**, *7*, 2483–2491. [CrossRef]

62. Reddy, C.V.; Koutavarapu, R.; Reddy, I.N.; Shim, J. Effect of a novel one-dimensional zinc tungsten oxide nanorods anchored two-dimensional graphitic carbon nitride nanosheets for improved solar-light-driven photocatalytic removal of toxic pollutants and photoelectrochemical water splitting. *J. Mat. Sci. Mat. El.* **2021**, *32*, 33–46. [CrossRef]

63. Seza, A.; Soleimani, F.; Naseri, N.; Soltaninejad, M.; Montazeri, S.M.; Sadrnezhaad, S.K.; Mohammadi, M.R.; Moghadam, H.A.; Forouzandeh, M.; Amin, M.H. Novel microwave-assisted synthesis of porous g-C$_3$N$_4$/SnO$_2$ nanocomposite for solar water-splitting. *Appl. Surf. Sci.* **2018**, *440*, 153–161. [CrossRef]

64. Bakr, A.E.A.; El Rouby, W.M.A.; Khan, M.D.; Farghali, A.A.; Xulu, B.; Revaprasadu, N. Synthesis and characterization of Z-scheme α-Fe$_2$O$_3$ NTs/ruptured tubular g-C$_3$N$_4$ for enhanced photoelectrochemical water oxidation. *Sol. Energy* **2019**, *193*, 403–412. [CrossRef]

65. Alam, K.M.; Kumar, P.; Kar, P.; Thakur, U.K.; Zeng, S.; Cui, K.; Shankar, K. Enhanced charge separation in g-C$_3$N$_4$–BiOI heterostructures for visible light driven photoelectrochemical water splitting. *Nanoscale Adv.* **2019**, *1*, 1460–1471. [CrossRef]

66. Liu, C.; Wang, F.; Zhang, J.; Wang, K.; Qiu, Y.; Liang, Q.; Chen, Z. Efficient photoelectrochemical water splitting by g-C$_3$N$_4$/TiO$_2$ nanotube array heterostructures. *Nanomicro Lett.* **2018**, *10*, 37. [CrossRef]

67. Liu, Y.; Yu, Y.-X.; Zhang, W.-D. Photoelectrochemical study on charge transfer properties of nanostructured Fe$_2$O$_3$ modified by g-C$_3$N$_4$. *Int. J. Hydrogen Energy* **2014**, *39*, 9105–9113. [CrossRef]

68. Lei, N.; Li, J.; Song, Q.; Liang, Z. Construction of g-C$_3$N$_4$/BCN two-dimensional heterojunction photoanode for enhanced photoelectrochemical water splitting. *Int. J. Hydrogen Energy* **2019**, *44*, 10498–10507. [CrossRef]

69. Murugan, C.; Bhojanaa, K.B.; Ong, W.-J.; Jothivenkatachalam, K.; Pandikumar, A. Improving hole mobility with the heterojunction of graphitic carbon nitride and titanium dioxide via soft template process in photoelectrocatalytic water splitting. *Int. J. Hydrogen Energy* **2019**, *44*, 30885–30898. [CrossRef]

70. Murugan, C.; Karnan, M.; Sathish, M.; Pandikumar, A. Construction of heterostructure based on hierarchical Bi$_2$MoO$_6$ and g-C$_3$N$_4$ with ease for impressive performance in photoelectrocatalytic water splitting and supercapacitor. *Catal. Sci. Technol.* **2020**, *10*, 2427–2442. [CrossRef]

71. Mohammad, A.; Khan, M.E.; Karim, M.R.; Cho, M.H. Synergistically effective and highly visible light responsive SnO$_2$-g-C$_3$N$_4$ nanostructures for improved photocatalytic and photoelectrochemical performance. *Appl. Surf. Sci.* **2019**, *495*, 143432. [CrossRef]

72. Hao, H.; Lu, D.; Wang, Q. Photoelectrochemical study on charge separation mechanisms of Bi$_2$WO$_6$ quantum dots decorated g-C$_3$N$_4$. *Int. J. Hydrogen Energy* **2018**, *43*, 8824–8834. [CrossRef]

73. Mahala, C.; Sharma, M.D.; Basu, M. ZnO nanosheets decorated with graphite-like carbon nitride quantum dots as photoanodes in photoelectrochemical water splitting. *ACS Appl. Nano Mater.* **2020**, *3*, 1999–2007. [CrossRef]

74. Ma, X.; Zhang, J.; Wang, B.; Li, Q.; Chu, S. Hierarchical Cu$_2$O foam/g-C$_3$N$_4$ photocathode for photoelectrochemical hydrogen production. *Appl. Surf. Sci.* **2018**, *427*, 907–916. [CrossRef]

75. Liu, Y.; Zhang, J.; Li, X.; Yao, Z.; Zhou, L.; Sun, H.; Wang, S. Graphitic carbon nitride decorated with CoP nanocrystals for enhanced photocatalytic and photoelectrochemical H$_2$ evolution. *Energy Fuel* **2019**, *33*, 11663–11676. [CrossRef]

76. Murugan, C.; Abinav Nataraj, R.; Praveen Kumar, M.; Ravichandran, S.; Pandikumar, A. Enhanced charge transfer process of bismuth vanadate interleaved graphitic carbon nitride nanohybrids in mediator-free direct Z-scheme photoelectrocatalytic water splitting. *Chem. Sel.* **2019**, *4*, 4653–4663. [CrossRef]

77. Wang, R.; Yan, J.; Zu, M.; Yang, S.; Cai, X.; Gao, Q.; Fang, Y.; Zhang, S.; Zhang, S. Facile synthesis of interlocking g-C$_3$N$_4$/CdS photoanode for stable photoelectrochemical hydrogen production. *Electrochim. Acta* **2018**, *279*, 74–83. [CrossRef]

78. Miao, H.; Zhang, G.; Hu, X.; Mu, J.; Han, T.; Fan, J.; Zhu, C.; Song, L.; Bai, J.; Hou, X. A novel strategy to prepare 2D g-C$_3$N$_4$ nanosheets and their photoelectrochemical properties. *J. Alloys Compd.* **2017**, *690*, 669–676. [CrossRef]

79. Bian, H.; Wang, A.; Li, Z.; Li, Z.; Diao, Y.; Lu, J.; Li, Y.Y. g-C$_3$N$_4$-modified water-crystallized mesoporous SnO$_2$ for enhanced photoelectrochemical properties. *Part. Part. Syst. Charact.* **2018**, *35*, 1800155. [CrossRef]

80. Jiang, T.; Nan, F.; Zhou, J.; Zheng, F.; Weng, Y.; Cai, T.-Y.; Ju, S.; Xu, B.; Fang, L. Enhanced photocatalytic and photoelectrochemical performance of g-C$_3$N$_4$/BiVO$_4$ heterojunction: A combined experimental and theoretical study. *AIP Adv.* **2019**, *9*, 055225. [CrossRef]

81. Sariket, D.; Ray, D.; Baduri, S.; Ghosh, S.; Maity, A.; Bhattacharya, C. Synthesis of g-C$_3$N$_4$/InVO$_4$ semiconductor for improved photocatalytic and photoelectrochemical applications. *Electroanalysis* **2020**, *32*, 2535–2544. [CrossRef]

82. Kokane, S.B.; Sasikala, R.; Phase, D.M.; Sartale, S.D. In$_2$S$_3$ nanoparticles dispersed on g-C$_3$N$_4$ nanosheets: Role of heterojunctions in photo-induced charge transfer and photoelectrochemical and photocatalytic performance. *J. Mater. Sci.* **2017**, *52*, 7077–7090. [CrossRef]

83. Zhang, S.; Yan, J.; Yang, S.; Xu, Y.; Cai, X.; Li, X.; Zhang, X.; Peng, F.; Fang, Y. Electrodeposition of Cu$_2$O/g-C$_3$N$_4$ heterojunction film on an FTO substrate for enhancing visible light photoelectrochemical water splitting. *Chin. J. Catal.* **2017**, *38*, 365–371. [CrossRef]

84. Wu, F.; Ma, Y.; Hu, Y.H. Near infrared light-driven photoelectrocatalytic water splitting over P-doped g-C$_3$N$_4$. *ACS Appl. Energy Mater.* **2020**, *3*, 11223–11230. [CrossRef]

85. Safaei, J.; Ullah, H.; Mohamed, N.A.; Mohamad Noh, M.F.; Soh, M.F.; Tahir, A.A.; Ahmad Ludin, N.; Ibrahim, M.A.; Wan Isahak, W.N.R.; Mat Teridi, M.A. Enhanced photoelectrochemical performance of Z-scheme g-C$_3$N$_4$/BiVO$_4$ photocatalyst. *Appl. Catal. B* **2018**, *234*, 296–310. [CrossRef]

86. Ragupathi, V.; Raja, M.A.; Panigrahi, P.; Ganapathi Subramaniam, N. CuO/g-C$_3$N$_4$ nanocomposite as promising photocatalyst for photoelectrochemical water splitting. *Optik* **2020**, *208*, 164569. [CrossRef]

87. Xiaoyi, H.; Xiangkang, Z.; Yue, L.; Jun, L.; Shi, Y.; Yichun, Y.; Jian, H.; David, T.M.; Xiwang, Z. Nano-layer based 1T-rich MoS$_2$/g-C$_3$N$_4$ co-catalyst system for enhanced photocatalytic and photoelectrochemical activity. *Appl. Catal. B* **2020**, *268*, 118466.

88. Guru, S.; Kumar, S.; Bellamkonda, S.; Gangavarapu, R.R. Synthesis of CuTi-LDH supported on g-C$_3$N$_4$ for electrochemical and photoelectrochemical oxygen evolution reactions. *Int. J. Hydrogen Energy* **2021**, *46*, 16414–16430. [CrossRef]

89. Guigoz, V.; Balan, L.; Aboulaich, A.; Schneider, R.; Gries, T. Heterostructured thin LaFeO$_3$/g-C$_3$N$_4$ films for efficient photoelectrochemical hydrogen evolution. *Int. J. Hydrogen Energy* **2020**, *45*, 17468–17479. [CrossRef]

90. Chen, Z.; Ma, G.; Chen, Z.; Zhang, Y.; Zhang, Z.; Gao, J.; Meng, Q.; Yuan, M.; Wang, X.; Liu, J.-M.; et al. Fabrication and photoelectrochemical properties of silicon nanowires/g-C$_3$N$_4$ core/shell arrays. *Appl. Surf. Sci.* **2017**, *396*, 609–615. [CrossRef]

91. Babu, B.; Shim, J.; Yoo, K. Efficient solar-light-driven photoelectrochemical water oxidation of one-step in-situ synthesized Co-doped g-C$_3$N$_4$ nanolayers. *Ceram. Int.* **2020**, *46*, 16422–16430. [CrossRef]

92. Arif, M.; Yasin, G.; Shakeel, M.; Mushtaq, M.A.; Ye, W.; Fang, X.; Ji, S.; Yan, D. Hierarchical CoFe-layered double hydroxide and g-C$_3$N$_4$ heterostructures with enhanced bifunctional photo/electrocatalytic activity towards overall water splitting. *Mater. Chem. Front.* **2019**, *3*, 520–531. [CrossRef]

93. Fang, Y.; Huang, W.; Yang, S.; Zhou, X.; Ge, C.; Gao, Q.; Fang, Y.; Zhang, S. Facile synthesis of anatase/rutile TiO$_2$/g-C$_3$N$_4$ multi-heterostructure for efficient photocatalytic overall water splitting. *Int. J. Hydrogen Energy* **2020**, *45*, 17378–17387. [CrossRef]

94. Bhandary, N.; Singh, A.P.; Kumar, S.; Ingole, P.P.; Thakur, G.S.; Ganguli, A.K.; Basu, S. In-situ solid-state synthesis of a AgNi/g-C$_3$N$_4$ nanocomposite for enhanced photoelectrochemical and photocatalytic activity. *ChemSusChem* **2016**, *9*, 2816–2823. [CrossRef] [PubMed]

95. Liu, W.; Shen, J.; Yang, X.; Liu, Q.; Tang, H. Dual Z-scheme g-C$_3$N$_4$/Ag$_3$PO$_4$/Ag$_2$MoO$_4$ ternary composite photocatalyst for solar oxygen evolution from water splitting. *Appl. Surf. Sci.* **2018**, *456*, 369–378. [CrossRef]

96. Babu, B.; Koutavarapu, R.; Shim, J.; Yoo, K. Enhanced visible-light-driven photoelectrochemical and photocatalytic performance of Au-SnO$_2$ quantum dot-anchored g-C$_3$N$_4$ nanosheets. *Sep. Pur. Technol.* **2020**, *240*, 116652. [CrossRef]

97. Li, J.; Yuan, H.; Zhu, Z. Improved photoelectrochemical performance of Z-scheme g-C$_3$N$_4$/Bi$_2$O$_3$/BiPO$_4$ heterostructure and degradation property. *Appl. Surf. Sci.* **2016**, *385*, 34–41. [CrossRef]

98. Chaudhary, D.; Kumar, S.; Khare, N. Boosting the visible-light photoelectrochemical performance of C$_3$N$_4$ by coupling with TiO$_2$ and carbon nanotubes: An organic/inorganic hybrid photocatalyst nanocomposite for photoelectrochemical water spitting. *Int. J. Hydrogen Energy* **2020**, *45*, 30091–30100. [CrossRef]

99. Si, H.; Deng, Q.; Yin, C.; Tavakoli, M.M.; Zhang, J.; Kong, J. Graphdiyne coupled with g-C$_3$N$_4$/NiFe-layered double hydroxide, a layered nanohybrid for highly efficient photoelectrochemical water oxidation. *Adv. Mater. Inter.* **2020**, *7*, 1902083. [CrossRef]

100. Gopalakrishnan, S.; Bhalerao, G.M.; Jeganathan, K. SrTiO$_3$ NPs/g-C$_3$N$_4$ NSs coupled Si NWs based hybrid photocathode for visible light driven photoelectrochemical water reduction. *ACS Sustain. Chem. Eng.* **2019**, *7*, 13911–13919. [CrossRef]

101. Alam, K.M.; Kumar, P.; Kar, P.; Goswami, A.; Thakur, U.K.; Zeng, S.; Vahidzadeh, E.; Cui, K.; Shankar, K. Heterojunctions of halogen-doped carbon nitride nanosheets and BiOI for sunlight-driven water-splitting. *Nanotechnology* **2019**, *31*, 084001. [CrossRef]

102. Wu, Y.; Song, M.; Chai, Z.; Wang, X. Assembling Bi$_2$MoO$_6$/Ru/g-C$_3$N$_4$ for highly effective oxygen generation from water splitting under visible-light irradiation. *Inorg. Chem.* **2019**, *58*, 7374–7384. [CrossRef] [PubMed]

103. Patnaik, S.; Swain, G.; Parida, K.M. Highly efficient charge transfer through a double Z-scheme mechanism by a Cu-promoted MoO$_3$/g-C$_3$N$_4$ hybrid nanocomposite with superior electrochemical and photocatalytic performance. *Nanoscale* **2018**, *10*, 5950–5964. [CrossRef] [PubMed]

104. Wen, P.; Sun, Y.; Li, H.; Liang, Z.; Wu, H.; Zhang, J.; Zeng, H.; Geyer, S.M.; Jiang, L. A highly active three-dimensional Z-scheme ZnO/Au/g-C$_3$N$_4$ photocathode for efficient photoelectrochemical water splitting. *Appl. Catal. B* **2020**, *263*, 118180. [CrossRef]

105. Xiao, J.; Zhang, X.; Li, Y. A ternary g-C$_3$N$_4$/Pt/ZnO photoanode for efficient photoelectrochemical water splitting. *Int. J. Hydrogen Energy* **2015**, *40*, 9080–9087. [CrossRef]

106. Liu, Y.; Su, F.-Y.; Yu, Y.-X.; Zhang, W.-D. Nano g-C$_3$N$_4$ modified Ti-Fe$_2$O$_3$ vertically arrays for efficient photoelectrochemical generation of hydrogen under visible light. *Int. J. Hydrogen Energy* **2016**, *41*, 7270–7279. [CrossRef]

107. Shanker, G.S.; Bhosale, R.; Ogale, S.; Nag, A. 2D nanocomposite of g-C$_3$N$_4$ and TiN embedded N-doped graphene for photoelectrochemical reduction of water using sunlight. *Adv. Mater. Inter.* **2018**, *5*, 1801488. [CrossRef]

108. Li, Y.; Wang, R.; Li, H.; Wei, X.; Feng, J.; Liu, K.; Dang, Y.; Zhou, A. Efficient and stable photoelectrochemical seawater splitting with TiO$_2$@g-C$_3$N$_4$ nanorod arrays decorated by Co-Pi. *J. Phys. Chem. C* **2015**, *119*, 20283–20292. [CrossRef]

109. Mahvelati-Shamsabadi, T.; Goharshadi, E.K.; Karimi-Nazarabad, M. Z-scheme design of Ag@g-C$_3$N$_4$/ZnS photoanode device for efficient solar water oxidation: An organic-inorganic electronic interface. *Int. J. Hydrogen Energy* **2019**, *4*, 13085–13097. [CrossRef]

110. Kumar, P.; Thakur, U.K.; Alam, K.; Kar, P.; Kisslinger, R.; Zeng, S.; Patel, S.; Shankar, K. Arrays of TiO$_2$ nanorods embedded with fluorine doped carbon nitride quantum dots (CNFQDs) for visible light driven water splitting. *Carbon* **2018**, *137*, 174–187. [CrossRef]

111. Li, K.; Huang, Z.; Zeng, X.; Huang, B.; Gao, S.; Lu, J. Synergetic effect of Ti3+ and oxygen doping on enhancing photoelectrochemical and photocatalytic properties of TiO$_2$/g-C$_3$N$_4$ heterojunctions. *ACS Appl. Mater. Inter.* **2017**, *9*, 11577–11586. [CrossRef] [PubMed]

112. Yu, Z.; Li, Y.; Qu, J.; Zheng, R.; Cairney, J.M.; Zhang, J.; Zhu, M.; Khan, A.; Li, W. Enhanced photoelectrochemical water-splitting performance with a hierarchical heterostructure: Co$_3$O$_4$ nanodots anchored TiO$_2$@P-C$_3$N$_4$ core-shell nanorod arrays. *Chem. Eng. J.* **2021**, *404*, 126458. [CrossRef]

113. Nayak, S.; Parida, K.M. Deciphering Z-scheme charge transfer dynamics in heterostructure NiFe-LDH/N-rGO/g-C$_3$N$_4$ nanocomposite for photocatalytic pollutant removal and water splitting reactions. *Sci. Rep.* **2019**, *9*, 2458. [CrossRef]

114. Naseer, I.; Adeel, A.; Ibrahim, K.; Muhammad, S.K.; Ahsanulhaq, Q. Molybdenum impregnated g-C3N4 nanotubes as potentially active photocatalyst for renewable energy applications. *Sci. Rep.* **2021**, *11*, 16886.

115. Guangqing, L.; Mengwei, X.; Qinpu, L.; Hui, Y.; Yuming, Z. Facile synthesis of C-doped hollow spherical g-C$_3$N$_4$ from supramolecular self-assembly for enhanced photoredox water splitting. *Int. J. Hydrogen Energy* **2019**, *44*, 25671–25679.

116. Ahmed, E.A.A.; Waleed, M.A.E.R.; Malik, D.K.; Ahmed, A.F.; Neerish, R. ZnCr-CO$_3$ LDH/ruptured tubular g-C$_3$N$_4$ composite with increased specific surface area for enhanced photoelectrochemical water splitting. *Appl. Surf. Sci.* **2020**, *508*, 145100.

117. Fazal, R.; Muhammad, H.; Asad, A.; Tingting, W.; Abbas, K.; Qiuyun, F.; Wei, L.; Heping, Z.; Zhiping, Z.; Bilawal, K.; et al. Synthesis of S-Doped porous g-C$_3$N$_4$ by using ionic liquids and subsequently coupled with Au-TiO$_2$ for exceptional cocatalyst-free visible-light catalytic activities. *Appl. Catal. B* **2018**, *237*, 1082–1090.